J. Fluid Mech. (2016), *vol.* 806, *pp.* 506–541.
doi:10.1017/jfm.2016.595

Experimental and theoretical study of wind turbine wakes in yawed conditions

Majid Bastankhah[1] **and Fernando Porté-Agel**[1,†]

[1]Wind Engineering and Renewable Energy Laboratory (WIRE), École Polytechnique Fédérale de Lausanne (EPFL), EPFL-ENAC-IIE-WIRE, 1015 Lausanne, Switzerland

(Received 23 March 2016; revised 25 July 2016; accepted 7 September 2016; first published online 14 October 2016)

This work is dedicated to systematically studying and predicting the wake characteristics of a yawed wind turbine immersed in a turbulent boundary layer. To achieve this goal, wind tunnel experiments were performed to characterize the wake of a horizontal-axis wind turbine model. A high-resolution stereoscopic particle image velocimetry system was used to measure the three velocity components in the turbine wake under different yaw angles and tip-speed ratios. Moreover, power and thrust measurements were carried out to analyse the performance of the wind turbine. These detailed wind tunnel measurements were then used to perform a budget study of the continuity and Reynolds-averaged Navier–Stokes equations for the wake of a yawed turbine. This theoretical analysis revealed some notable features of the wakes of yawed turbines, such as the asymmetric distribution of the wake skew angle with respect to the wake centre. Under highly yawed conditions, the formation of a counter-rotating vortex pair in the wake cross-section as well as the vertical displacement of the wake centre were shown and analysed. Finally, this study enabled us to develop general governing equations upon which a simple and computationally inexpensive analytical model was built. The proposed model aims at predicting the wake deflection and the far-wake velocity distribution for yawed turbines. Comparisons of model predictions with the wind tunnel measurements show that this simple model can acceptably predict the velocity distribution in the far wake of a yawed turbine. Apart from the ability of the model to predict wake flows in yawed conditions, it can provide valuable physical insight on the behaviour of turbine wakes in this complex situation.

Key words: turbulent flows, turbulent boundary layers, wakes/jets

1. Introduction

In order to address the increasing demand of wind energy production, researchers seek ways to improve the efficiency of existing and future wind farms. The most important cause of power losses in wind farms is the fact that turbines usually operate in the wakes of upwind ones. Yaw angle control is one of the methods that could be used to alleviate this situation by deflecting the wakes away from downwind turbines (Dahlberg & Medici 2003). Even though yawing a turbine reduces its power production, it can potentially increase the total power generated by the whole wind farm.

† Email address for correspondence: fernando.porte-agel@epfl.ch

To assess the viability of yaw-angle control strategies, a better understanding of the wakes of yawed turbines is crucial. Most of the previous studies of yawed turbines are limited to the performance of the turbine or the near-wake characteristics (e.g. Grant, Parkin & Wang 1997; Grant & Parkin 2000; Haans *et al.* 2005; Haans, van Kuik & van Bussel 2007; Sant 2007; Krogstad & Adaramola 2012; Micallef *et al.* 2013). Yawed turbines and their near wakes have also benefited from extensive studies of flow through helicopter rotors in forward flight as they are conceptually similar (e.g. Coleman, Feingold & Stempin 1945).

Studies of the far wakes of yawed turbines, by contrast, have received rather little attention. In some of the early studies, Dahlberg & Medici (2003) and later Medici & Alfredsson (2006) quantified the far-wake velocity distribution at a few downwind locations for a yawed turbine located in a uniform flow. Their wind tunnel measurements confirmed that yawing the turbine can be used as a promising method to manipulate turbine wakes and mitigate their effects on downwind turbines. Later, Jiménez, Crespo & Migoya (2010) used large-eddy simulation (LES) to investigate the deflection of wakes of yawed turbines with different thrust coefficients. They pointed out that, for a given yaw angle, the wake deflects more for turbines with higher thrust coefficients. Recently, Fleming *et al.* (2014) also used LES to study the wake of a turbine in yawed conditions and showed that yawing a turbine is an effective method to redirect its wake.

Even though these numerical simulations and wind tunnel measurements showed the potential of yaw-angle control, due to their high computational or measurement costs, they cannot be employed to fully assess the capability of this strategy under the wide variety of conditions that have to be considered for the optimum design and operation of wind farms. For example, wind farms are continuously exposed to change in mean wind magnitude and direction, ambient turbulence, thermal stability and wind turbine characteristics (Porté-Agel, Wu & Chen 2013). Therefore, simple and inexpensive models that can predict the wakes of yawed turbines with an acceptable accuracy are still needed. Jiménez *et al.* (2010) assumed a top-hat profile for the wake velocity deficit and developed a simple formula to predict the wake deflection angle based on the conservation of mass and momentum for a control volume around the turbine. Based on this study, the wake skew angle θ is determined by

$$\theta = \frac{\sin\gamma C_T}{2\left(1+\zeta\dfrac{x}{d}\right)^2}, \tag{1.1}$$

where γ denotes the yaw angle, x is the downwind distance, d is the rotor diameter and ζ is the wake growth rate for the top-hat velocity-deficit profile which was chosen to be 0.1 for $\gamma = 10°$, $20°$ and 0.125 for $\gamma = 30°$ (Jiménez *et al.* 2010). In (1.1) and the remainder of this paper, the yaw angle γ is positive in the clockwise direction, and θ is positive in the counter-clockwise direction, seen from the top. Note that the apparent difference between (1.1) and the formula in the original work is due to the different definitions used for the thrust coefficient of the turbine C_T. In the current study, C_T is defined as

$$C_T = \frac{T}{0.5\rho\left(\dfrac{\pi}{4}d^2\right)\bar{u}_h^2}, \tag{1.2}$$

where T is the total force exerted on the turbine by the incoming wind, ρ is the air density and $\bar{u}_h$ is the incoming velocity at the hub height of the turbine.

Later, Gebraad *et al.* (2014) integrated (1.1) to find the wake-centre trajectory for a yawed turbine. They also used the top-hat model suggested by Jensen (1983) to describe the wake velocity, although the applicability of this model for wakes of yawed turbines is questionable.

Most of the aforementioned studies on far wakes of yawed turbines have been done from a pragmatic point of view. In other words, they essentially aimed at finding the amount of the wake deflection in different conditions, and whether or not the yaw-angle control can improve the wind farm power production. Despite the merit of those studies, many valuable insights could emerge from a more in-depth theoretical analysis of turbine wakes in yawed conditions. In addition to providing a better understanding, such theoretical analysis can ultimately help us develop more robust and accurate analytical models.

In the present work, detailed wind tunnel measurements are used to study the wake of a yawed wind turbine placed in a neutrally stratified boundary layer. Highly spatially resolved velocity measurements, together with thrust and power measurements, enable us to systematically study the interaction of the wake of the model turbine with the incoming turbulent boundary layer. These experimental data are then taken to study the budget of the steady-state continuity and Reynolds-averaged Navier–Stokes (RANS) equations. This budget study reveals some valuable features of turbine wakes in yawed conditions. In addition, the simplification of RANS equations results in the approximate governing equations upon which an inexpensive analytical model is built. This analytical model intends to acceptably predict the velocity distribution in the wake of a yawed turbine under different conditions.

The remainder of this paper is organized as follows. In § 2, the experimental set-up and some key measurements are shown. The budget study of governing equations is then presented in § 3. Section 4 is dedicated to examining the self-similarity for wakes of yawed turbines. An analytical model for the prediction of the far-wake velocity is then developed in § 5, and the required wake characteristics in the onset of the far-wake region are specified in § 6. The model predictions and the comparison with wind tunnel measurements are shown in § 7. Finally, a summary is presented in § 8.

2. Wind tunnel measurements

Experiments were performed in the new closed-loop boundary-layer wind tunnel at the WIRE Laboratory of EPFL. The test section, designed for atmospheric boundary-layer studies, is 2.0 m high, 2.6 m wide and 28 m long. There is a contraction with a 5:1 area ratio upwind of the test section, and the tunnel is driven by a 130 kW fan. The turbulence intensity in the centre of the wind tunnel (free stream) is lower than 0.1 %. The turbulent boundary layer is naturally developed over the wind tunnel floor thanks to the long test section. In the current study, the measurements were performed approximately 22 m downstream of the test section entrance. The time-averaged incoming velocity at the hub height of the turbine $\bar{u}_h$ is kept constant at 4.88 m s^{-1}. Figure 1(*a*,*b*) shows the vertical profiles of the normalized mean streamwise velocity $\bar{u}/\bar{u}_h$ and the streamwise turbulence intensity I in the boundary layer in absence of the turbine obtained with hot-wire anemometry. The boundary-layer thickness is approximately 0.4 m at the turbine location. The aerodynamic surface roughness length and the friction velocity were found to be $z_0 = 0.022$ mm and $u_* = 0.19$ m s^{-1}, respectively, based on fitting a logarithmic velocity profile to the measured velocity profile in the surface layer (approximately lowest 15 % of the boundary layer) as shown in figure 1(*c*).

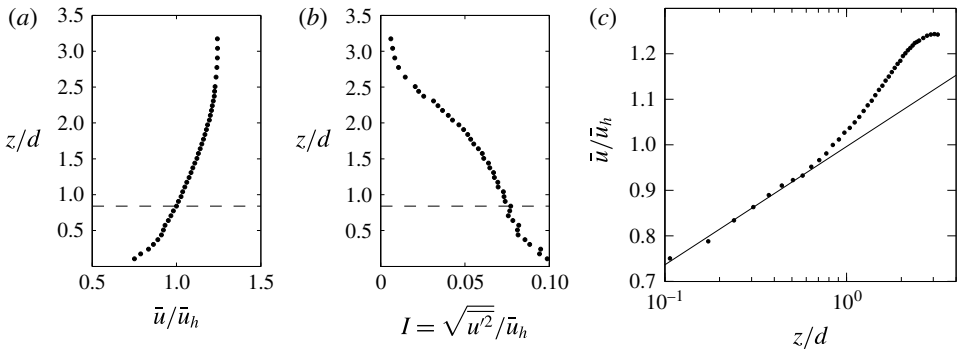

FIGURE 1. Characteristics of the incoming turbulent boundary layer: (*a*) the normalized mean streamwise velocity profile, and (*b*) the streamwise turbulence intensity profile. The horizontal dashed lines represent the turbine hub height. (*c*) The normalized mean streamwise velocity profile in a semi-logarithmic scale. The solid line shows the fitted logarithmic profile.

A high-resolution stereoscopic particle image velocimetry (S-PIV) system from LaVision was used to measure three velocity components downstream of the turbine in the horizontal plane at hub height, i.e. xy plane, where x and y denote streamwise and spanwise directions, respectively. Two 29MP 12-bit charge-coupled device (CCD) cameras (6600×4400 pixels) together with 105 mm lenses were installed on Scheimpflug mountings to maximize the focused area in the field of view (FOV). The area and spatial resolution of the FOV are $4d \times 2.5d$ and $0.015d$, respectively, where d is the diameter of the wind turbine (15 cm). Data were sampled at a frequency of 1 Hz. The measurements were performed in three FOVs with some overlapping to capture the wake flow in a broad streamwise range from the near-wake ($0.4d$) to the far-wake region ($12d$). The mean velocity field was obtained by ensemble averaging 800 to 1000 instantaneous velocity fields. In addition to this PIV set-up, S-PIV measurements were performed in planes normal to the incoming flow (i.e. yz planes, where z denotes the vertical direction) at few selected downwind locations, mainly to study the structure of the wake cross-section under yawed conditions. Two 16-bit sCMOS cameras (2560×2160 pixels) were used to capture the wake flow in FOVs with the size of $3d \times 2d$ and the spatial resolution of $0.023d$. Data were sampled at a frequency of 10 Hz. The mean velocity field was obtained by ensemble averaging 1200 instantaneous velocity fields.

The model wind turbine used in this experiment was designed and built at the WIRE laboratory of EPFL. This horizontal-axis turbine is three bladed, with a diameter of 15 cm. The blade profile is a 5 % thick plate with a 5 % circular arc camber. The height of the turbine hub above the floor is 12.5 cm. The blockage ratio of the wind turbine model to the wind tunnel cross-sectional area is less than 0.004, indicating that the confinement effect of the wind tunnel walls on the turbine wake is negligible. The turbine rotor drives a small direct current (DC) generator to extract the energy from the wind. The tower of the turbine was mounted on a multi-axis strain gauge sensor to measure the thrust force exerted by the wind on the model turbine. The tip-speed ratio was also varied by applying different electrical loads on the generator attached to the turbine rotor.

Figure 2 shows the variation of the thrust coefficient C_T and power coefficient C_p of the wind turbine versus tip-speed ratio for different yaw angles. The value of C_T

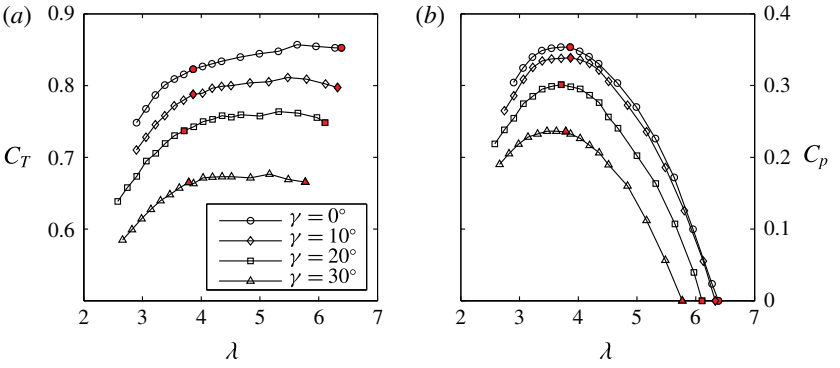

FIGURE 2. Turbine performance versus tip-speed ratio (thrust coefficient C_T (*a*) and power coefficient C_p (*b*)) for different yaw angles: $\gamma = 0°$ (circle), $\gamma = 10°$ (diamond), $\gamma = 20°$ (square), and $\gamma = 30°$ (triangle). For red coloured points, PIV measurements were performed.

is calculated by (1.2) and C_p is calculated by

$$C_p = \frac{Q\Omega}{0.5\rho\left(\frac{\pi}{4}d^2\right)\bar{u}_h^3}, \tag{2.1}$$

where Q is the torque generated by the rotor, and Ω is the rotational velocity of the rotor. The value of the generated torque Q is estimated by multiplying the generated electrical current by the torque constant of the DC-generator. The rotational velocity Ω is measured by the digital encoder attached to the DC-generator.

Figure 2 shows that both the thrust force and the generated power clearly decrease as the yaw angle increases which is expected and in agreement with previous studies (e.g. Krogstad & Adaramola 2012).

For each yaw angle, the wake-flow measurements were performed for two different tip-speed ratios: (i) the tip-speed ratio of the turbine when the electrical circuit connected to the generator is open, so the turbine rotates freely. This tip-speed ratio is called λ_f later on in this paper. (ii) The tip-speed ratio at which the turbine has the maximum power production, and it is called the optimal tip-speed ratio λ_o in the following. λ_f and λ_o for each yaw angle are indicated in figure 2 with red coloured points. For the sake of brevity, however, the following discussions will focus mostly on the data related to the optimal tip-speed ratio λ_o, unless otherwise stated.

Figure 3 shows contours of the normalized mean streamwise velocity $\bar{u}/\bar{u}_h$ for different yaw angles ($\gamma = 0°$, 10°, 20° and 30°) in the horizontal plane at hub height. It can be seen that the wake velocity deficit reduces as the yaw angle increases because of the reduction in the total thrust force of the turbine (see figure 2). White dots in the figure show the loci of the maximum velocity deficit in the measured PIV plane at different downwind locations. As expected, the wake deflection increases with the increase of yaw angle. The black lines in the figure show the initial wake deflection predicted by Coleman *et al.* (1945). This study is further discussed in § 6. Moreover, the white lines in figure 3 show the wake deflection predicted by the work of Jiménez *et al.* (2010), described by equation (1.1). As shown in the figure, this model considerably overestimates the wake trajectory for all cases. One can indeed improve the predictions by empirically adjusting the coefficient ζ in (1.1) for each case. However, this case specificity highlights the need for more realistic and robust modelling of turbine wakes in yawed conditions.

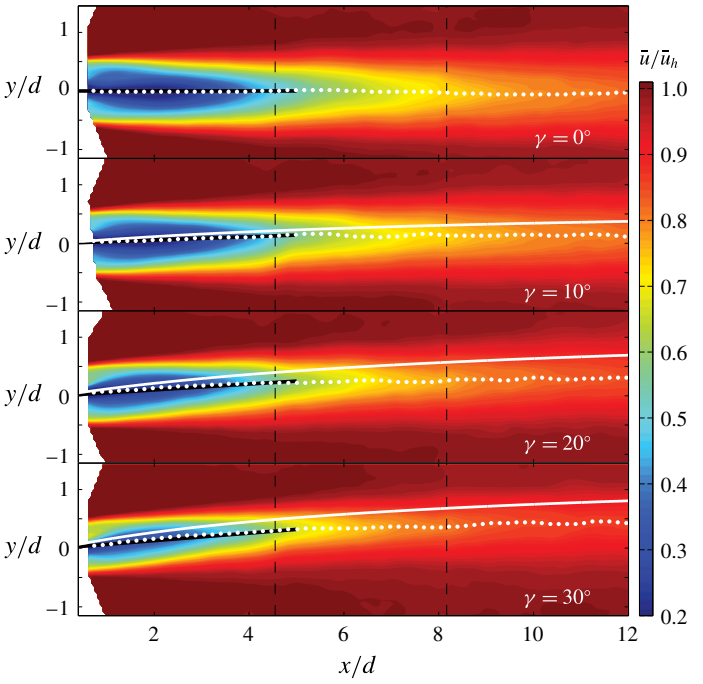

FIGURE 3. Contours of the normalized mean streamwise velocity $\bar{u}/\bar{u}_h$ in the horizontal plane at hub height downwind of a turbine for different yaw angles ($\gamma = 0°$, 10°, 20° and 30°) at $\lambda = \lambda_o$. White dots and white lines represent the wake-centre trajectory in the horizontal plane obtained from the wind tunnel measurements and Jiménez *et al.* (2010) (1.1), respectively. Black lines show the initial wake deflection predicted by Coleman *et al.* (1945) (6.12). Overlapped locations of PIV planes are indicated by vertical dashed lines.

Although it is difficult to accurately predict the wake deflection, its cause can be explained simply by the conservation of momentum. A yawed turbine exerts a lateral force on the incoming airflow. Based on momentum conservation, this lateral force induces a spanwise wake velocity. This can be confirmed by figure 4 that shows contours of the normalized spanwise velocity $\bar{v}/\bar{u}_h$ for two different yaw angles ($\gamma = 0°$ and 30°). As a result of this strong spanwise velocity distribution, the wake of a yawed turbine deflects to one side. It is also interesting to note that the peak of spanwise velocity surprisingly does not occur where the streamwise velocity deficit is maximum. This will be elucidated in the following section. In fact, it will be shown later in § 3.2 that, based on the budget study of RANS equations, the spanwise velocity distribution has to be asymmetric with respect to the wake centre.

Next, figure 5 shows contours of the normalized velocity deficit $\Delta\bar{u}/\bar{u}_h$ overlaid with vectors of in-plane velocity components in four yz planes located at different downwind locations ($x/d = 2$, 4, 6 and 8) for five different yaw angles ($\gamma = 0°$, 10°, 20°, 30° and −30°). The wake centre, defined as the point where the velocity deficit is maximum at each downwind location, is also shown by white dots in the figure.

As seen in the figure, a counter-rotating vortex pair (CVP) is formed as the wake moves downstream for higher yaw angles, so the wake has a kidney-shaped cross-section in the far-wake region. In addition to the current study, this kidney-shaped cross-section has been very recently reported for the wake of a yawed porous disk in uniform flows performed by Howland *et al.* (2016). However, no explanation

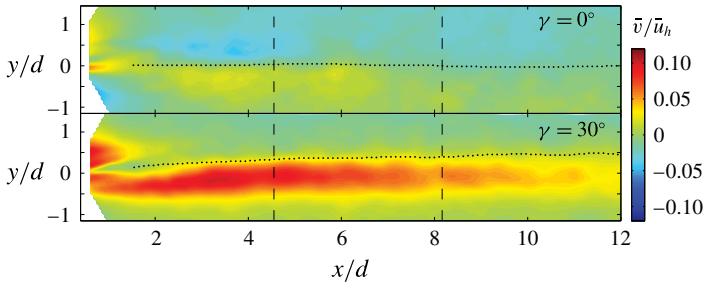

FIGURE 4. Contours of the normalized mean spanwise velocity ($\bar{v}/\bar{u}_h$) in the horizontal plane at hub height downwind of a turbine for two different yaw angles ($\gamma = 0°$, and 30°) at $\lambda = \lambda_o$. Black dots represent the wake centre trajectory in the horizontal plane, and overlapped locations of PIV planes are indicated by vertical dashed lines.

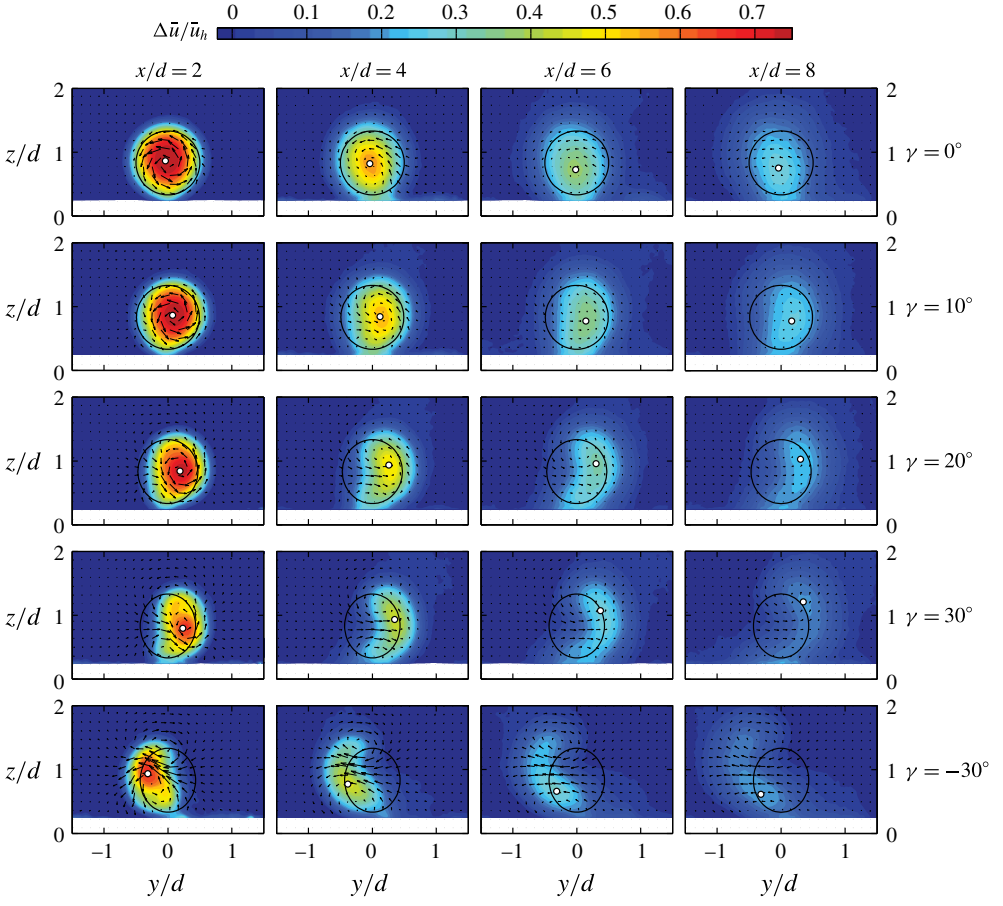

FIGURE 5. Contours of the normalized streamwise velocity deficit in yz planes at different downwind locations and different yaw angles for a turbine operating at $\lambda = \lambda_o$. Black circles indicate the frontal area of the wind turbine and white dots represent the wake-centre position at each downwind location. The vector field represents the in-plane velocity components.

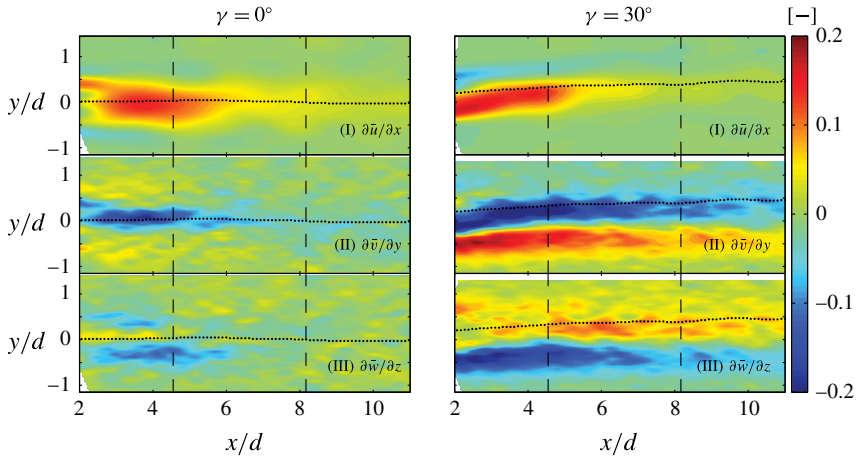

FIGURE 6. Contours of the terms of the mean continuity equation (3.1) in the horizontal plane at hub height for two different yaw angles ($\gamma = 0°$, and 30°) at $\lambda = \lambda_o$. Contours are non-dimensionalized with $\bar{u}_h$ and d. Black dots represent the locus of the maximum velocity deficit in the measured plane, and overlapped locations of PIV planes are indicated by vertical dashed lines.

regarding the formation mechanism of the CVP was provided in the mentioned study. The budget study of mean continuity equation will be employed in § 3.1 to explain the mechanism leading to the CVP under highly yawed conditions. Moreover, the wake centre is observed to move vertically for high yaw angles (e.g. $\gamma = 30°$) and, more interestingly, the direction of this vertical displacement depends on the yaw-angle direction. This will be elaborated in § 3.1.

3. Governing equations

3.1. *Continuity equation*

The mean continuity equation is

$$\underbrace{\frac{\partial \bar{u}}{\partial x}}_{\text{(I)}} + \underbrace{\frac{\partial \bar{v}}{\partial y}}_{\text{(II)}} + \underbrace{\frac{\partial \bar{w}}{\partial z}}_{\text{(III)}} = 0, \tag{3.1}$$

where u, v and w are the streamwise, spanwise and vertical velocities, respectively, and the overbar denotes ensemble averaging. Figure 6 shows contours of the terms of (3.1) in the horizontal plane at hub height of a turbine operating at two different yaw angles ($\gamma = 0°$ and 30°). All the terms shown in the figure are normalized with respect to the averaged incoming velocity at hub height $\bar{u}_h$ and the rotor diameter d. Note that only variations in the x and y directions can be calculated with S-PIV measurements in a horizontal plane, so term (III) shown in figure 6 is calculated based on the fact that (3.1) has to be balanced. The figure shows that although the terms of (3.1) are of the same order of magnitude for the non-yawed turbine, terms (II) and (III) are considerably bigger than term (I) in the far-wake region under yawed conditions.

In the following, the scale analysis of (3.1) will be used to explain the fundamental difference between the structure of wakes under non-yawed versus yawed conditions.

The velocity scale $\tilde{u}_s$ for the variation of $\bar{u}$ can be defined as the maximum velocity deficit at each streamwise position (Tennekes & Lumley 1972). Thus, we can write $\partial\bar{u}/\partial x = O(\tilde{u}_s/L)$, where L denotes the scale of change in the x direction. Moreover, we define the velocity scale $\tilde{v}_s$ for the variation of $\bar{v}$ which is equal to the maximum value of $\bar{v}$ at each streamwise position. This leads to $\partial\bar{v}/\partial y = O(\tilde{v}_s/l)$, where l is the cross-stream scale, and $l/L \to 0$ in far wakes. One possibility is to assume that terms (I) and (II) in (3.1) are of the same order of magnitude which leads to the conclusion that $\tilde{v}_s = \tilde{u}_s l/L$. This means that $\tilde{v}_s$ is considerably smaller than $\tilde{u}_s$ in far wakes which occurs under non-yawed conditions (see figure 4). Equation (3.1) also implies that $\tilde{w}_s$, the velocity scale for the variation of $\bar{w}$, cannot be higher than $\tilde{u}_s l/L$ in this case.

For higher yaw angles, however, $\tilde{v}_s$ cannot be assumed negligible compared to $\tilde{u}_s$. As already discussed, based on momentum conservation, $\tilde{v}_s$ is generated due to the lateral component of the thrust force (i.e. $\approx T \sin\gamma$), whereas $\tilde{u}_s$ is due to the streamwise component of the thrust force (i.e. $\approx T\cos\gamma$). As a result, if the yaw angle is large enough (i.e. $\tan\gamma \to 1$), we can write $\tilde{v}_s \approx \tilde{u}_s$. In this case, term (II) in (3.1) is considerably bigger than term (I), and consequently it has to be balanced with term (III). In other words, the continuity equation in the far wake of a rotor with a high yaw angle is reduced to

$$\frac{\partial\bar{v}}{\partial y} + \frac{\partial\bar{w}}{\partial z} \approx 0. \tag{3.2}$$

Equation (3.2) states that the strong variation of $\bar{v}$ in the y direction that occurs in wakes of turbines with a high yaw angle results in a strong variation of $\bar{w}$ in the z direction, which in turn alters the shape of the wake cross-section. In fact, we hypothesize that the formation of the CVP presented in figure 5 can be explained with the analysis of (3.2). This is demonstrated in the schematic of the wake cross-section shown in figure 7. For the sake of simplicity, the incoming flow is assumed to be uniform and the wake rotation and ground effects are ignored for now but will be addressed later. In this regard, the horizontal line at the hub height can be considered as a symmetry line with $\bar{w} = 0$. Point A in figure 7 signifies the position where $\bar{v}$ is maximum and, as already seen in figure 4, it does not occur in the locus of the maximum velocity deficit shown by point C in figure 7. On the left side of point A (region I), $\partial\bar{v}/\partial y > 0$ and from (3.2), $\partial\bar{w}/\partial z < 0$. On the other hand, $\partial\bar{v}/\partial y < 0$ and $\partial\bar{w}/\partial z > 0$ on the right side of point A (region II). As a result, $\bar{w}$ becomes negative in region I and positive in region II. This spatial distribution of $\bar{v}$ and $\bar{w}$ induces flow rotation as shown by solid arrows in the figure. At the wake edge shown by the horizontal dotted line in the figure, the induced spanwise velocity $\bar{v}$ due to yawing the turbine becomes negligible, but the vertical component of velocity $\bar{w}$ is still non-zero and variable due to the flow rotation mentioned above. In order to satisfy continuity, the flow rotation has to be therefore complete, as shown by dotted arrows in the figure. With a similar argument, the presence of a counter-rotating vortex in the lower half of the wake cross-section can be expected.

A general conclusion that can be drawn by the aforementioned discussion is that any type of free shear flow with a strong variation of cross-wind velocity experiences the formation of CVP to satisfy the continuity. For instance, the presence of CVP in the cross-section of cross-flow jets can be justified similarly. Several different mechanisms for the formation of the CVP in cross-flow jets have been suggested in the literature (e.g. Broadwell & Breidenthal 1984; Kelso, Lim & Perry 1996; Cortelezzi & Karagozian 2001; Muppidi & Mahesh 2006; Marzouk & Ghoniem 2007).

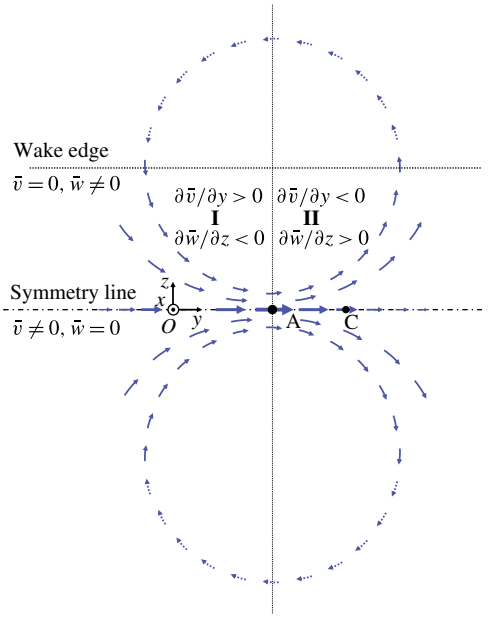

FIGURE 7. Schematic figure of the mechanism leading to the formation of the CVP.

See the review of Mahesh (2013) for more information in this context. However, to our best knowledge, it is the first time that mass conservation is used to explain the formation of the CVP. Indeed, it will be of great interest to further investigate the validity of our suggested mechanism leading to the CVP for other types of similar flows in future studies.

As mentioned earlier, the wake rotation and the presence of the ground are ignored in the idealized schematic figure of the wake cross-section shown in figure 7. In the following, we will examine how the CVP interacts with the ground and the wake rotation. For the sake of simplicity, we reduce the problem to a two-dimensional potential flow in the yz plane, where the CVP is modelled with counter-rotating vortices of strength Γ, and the wake rotation is modelled with a vortex of strength Γ'. Moreover, the presence of the ground is modelled by the method of images (see White (2009) for more information). By using the complex variable $\xi = y + \mathrm{i}z$, where $\mathrm{i} = (-1)^{1/2}$, the complex potential $f(\xi)$ for this problem can be written as

$$\begin{aligned} f(\xi) \;=\; & \frac{\mathrm{i}\Gamma}{2\pi}(-\ln(\xi-\xi_1)+\ln(\xi-\xi_2)+\ln(\xi-\bar{\xi}_1)-\ln(\xi-\bar{\xi}_2)) \\ & +\frac{\mathrm{i}\Gamma'}{2\pi}(-\ln(\xi-\xi_0)+\ln(\xi-\bar{\xi}_0)), \end{aligned} \tag{3.3}$$

where ξ_0, ξ_1 and ξ_2 are the positions of the wake centre and upper and lower vortices of the CVP, respectively, and the overbar denotes the complex conjugate. To find the velocities at each position, one can simply differentiate $f(\xi)$, so

$$\frac{\mathrm{d}f}{\mathrm{d}\xi} = v - \mathrm{i}w. \tag{3.4}$$

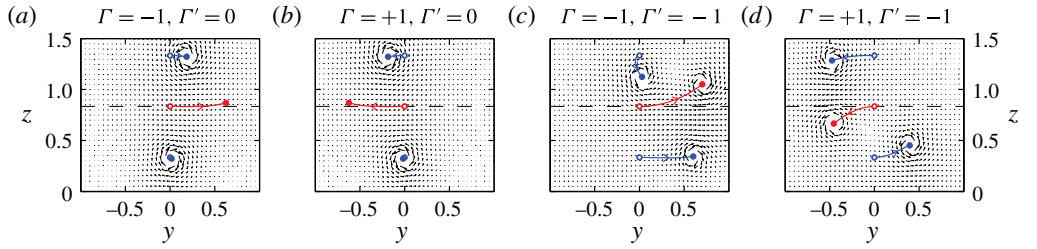

FIGURE 8. Wake-centre displacement predicted by the potential theory. Red curves show the displacement of the wake centre, and blue ones show the displacement of the CVP. The horizontal dashed lines indicate the initial position of the wake centre which is equal to the normalized turbine hub height z_h/d. The initial position of the pair of vortices is $z_h/d \pm 0.5$. Vectors show the flow field at $t = 1.5$ s.

It is worth recalling that the superposition of potential flow solutions implies that each vortex is displaced by the other vortices, so the velocity at each vortex centre is only due to the other vortices. Once the velocities are known, the vortices' displacements over time can be found by

$$\mathrm{d}\xi = \mathrm{d}y + \mathrm{i}\,\mathrm{d}z = \int_0^t v\,\mathrm{d}t + \mathrm{i}\int_0^t w\,\mathrm{d}t, \tag{3.5}$$

which can be solved numerically. The results are shown in figure 8 for different values of Γ and Γ' over an arbitrarily chosen time period of $t = 1.5$ s. For the given time period, the wake-centre's displacement is shown by a red curve in each figure, while the displacements of the CVP are indicated by blue curves. The initial vertical positions of vortices are selected rather similar to their real positions in wakes of yawed turbines. Note also that Γ and Γ' are assumed to be constant over the time for the sake of simplicity although both change in real situations.

In figure 8(*a*,*b*), the wake rotation is set to zero (i.e. $\Gamma' = 0$), so that the sole effect of the ground can be studied for both negative and positive Γ, which correspond to positive and negative yaw angles, respectively. The figures show that the wake centre tends to slightly move upward with the same magnitude for both positive and negative yaw angles. If the wake rotation is taken into account, figure 8(*c*,*d*), however, shows that the vertical displacement of the wake centre can be either upward or downward depending on the direction of the wake rotation with respect to the one of the CVP. As can be seen in the figures, the wake rotation makes the wake centre move upward if Γ and Γ' have the same sign, and *vice versa*. It is also interesting to note that the magnitude of the wake-centre displacement is smaller in both horizontal and vertical directions in figure 8(*d*) compared to the one in figure 8(*c*) which is consistent with the wind tunnel measurements shown in figure 5. This is due to the fact that the wake rotation and ground effects act against each other in figure 8(*d*). The accurate prediction of the wake-centre displacement for real situations is obviously not possible via this simple method based on the potential theory. However, the comparison of figures 5 and 8 reveals that the employed method can provide useful insights on the origin and behaviour of the wake-centre vertical displacement observed for wakes of turbines with high yaw angles.

The vertical displacement of the wake centre increases the net wake deflection under yawed conditions, which potentially can further mitigate wake effects on downwind

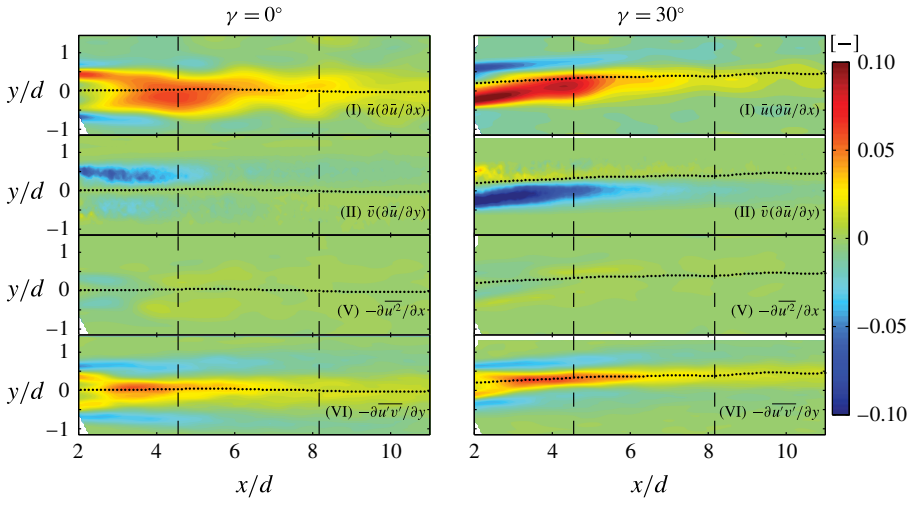

FIGURE 9. Contours of the terms of the x-RANS equation (3.6) measured in the horizontal plane at hub height for two different yaw angles ($\gamma = 0°$, and 30°) at $\lambda = \lambda_o$. Contours are non-dimensionalized with $\bar{u}_h^2$ and d. Black dots represent the locus of the maximum velocity deficit in the measured plane, and overlapped locations of PIV planes are indicated by vertical dashed lines.

turbines. As discussed earlier, the direction of this vertical displacement depends on the yaw-angle direction for rotating wakes (e.g. wind turbine wakes). The wake can therefore be pushed towards the ground if the yaw angle is selected accordingly. This situation might be favourable in very large wind farms as the kinetic energy is transferred mainly from higher regions in the boundary layer towards wind turbines (Cal *et al.* 2010; Calaf, Meneveau & Meyers 2010; Lu & Porté-Agel 2011; Abkar & Porté-Agel 2013). On the other hand, yawing the turbine in the opposite direction moves the wake upward which leads to a slightly bigger wake deflection as shown in figures 5 and 8. Moreover, the upward motion of the wake may reduce the shear in the incoming flow and lead to a more uniform flow, which in turn can reduce unsteady loads on the blades of downwind turbines. It is, therefore, unclear at this stage which yaw-angle direction is more suitable, but this topic definitely deserves more attention in future studies. Note also that the vertical displacement of the wake centre reduces with the decrease in yaw angle (see figure 5) simply because the CVP weakens for lower yaw angles.

3.2. *Reynolds-averaged Navier–Stokes (RANS) equations*

The RANS equation in the streamwise direction at high Reynolds numbers is (Pope 2000)

$$\underbrace{\bar{u}\frac{\partial\bar{u}}{\partial x}}_{\text{(I)}} + \underbrace{\bar{v}\frac{\partial\bar{u}}{\partial y}}_{\text{(II)}} + \underbrace{\bar{w}\frac{\partial\bar{u}}{\partial z}}_{\text{(III)}} = \underbrace{-\frac{1}{\rho}\frac{\partial\bar{p}}{\partial x}}_{\text{(IV)}} \underbrace{-\frac{\partial\overline{u'^2}}{\partial x}}_{\text{(V)}} \underbrace{-\frac{\partial\overline{u'v'}}{\partial y}}_{\text{(VI)}} \underbrace{-\frac{\partial\overline{u'w'}}{\partial z}}_{\text{(VII)}}, \tag{3.6}$$

where primes indicate turbulent fluctuations and p is the static pressure. Figure 9 shows contours of the terms in (3.6) measured in the horizontal plane at hub height for the wake of a turbine operating at two different yaw angles ($\gamma = 0°$ and 30°).

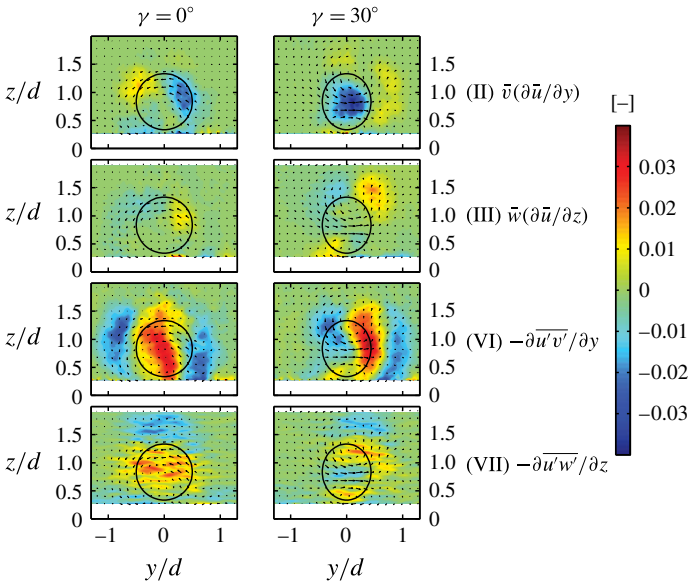

FIGURE 10. Contours of the terms of the x-RANS equation (3.6) measured in a yz plane at $x/d = 6$ for two different yaw angles ($\gamma = 0°$, and 30°) at $\lambda = \lambda_o$. Contours are non-dimensionalized with $\bar{u}_h^2$ and d. Black circles indicate the frontal area of the wind turbine. The vector field represents in-plane velocity components.

Additionally, the contours of the terms of (3.6) measured in a yz plane at $x/d = 6$ are shown in figure 10 for two different yaw angles ($\gamma = 0°$ and 30°). On the line of intersection of the xy and yz PIV planes, all the terms of (3.6) except the pressure one, term (IV), can be calculated. Figure 11 shows the lateral profiles of all the measured terms on the line of intersection at $x/d = 6$ for a turbine with $\gamma = 30°$. Firstly, the residual that is basically equal to the pressure term (term (IV)) in (3.6) is seen to be small. We, therefore, neglect this term compared to the dominant terms of (3.6) in the remainder of this paper. Secondly, figure 11 shows that terms (I), (II) and (VI) are bigger than the other terms at hub height. In order to quantify the change of these terms by moving downstream, the maximum of their normalized magnitude in the horizontal plane at hub height is plotted as a function of downwind distance in figure 12 for $\gamma = 0°$ and 30°. It can be seen that in the near wake of a yawed turbine, the convective terms are considerably higher than the shear stress term. The convective terms, however, diminish quickly as the wake moves downstream, and thus the shear stress becomes noteworthy in the far-wake region. In other words, the wake of a yawed turbine changes from a flow mostly dominated by gradients of mean velocities in the near wake to a turbulent free shear flow in the far wake, and it ultimately asymptotes to the wake of a non-yawed turbine.

Further analysis of (3.6) can reveal some important features of turbine wakes in yawed conditions. Multiplying the continuity equation (3.1) by $\bar{u}$ and then subtracting the resultant equation from (3.6) yields

$$\bar{v}\frac{\partial\bar{u}}{\partial y} - \bar{u}\frac{\partial\bar{v}}{\partial y} + \bar{w}\frac{\partial\bar{u}}{\partial z} - \bar{u}\frac{\partial\bar{w}}{\partial z} = -\frac{\partial\overline{u'^2}}{\partial x} - \frac{\partial\overline{u'v'}}{\partial y} - \frac{\partial\overline{u'w'}}{\partial z}. \tag{3.7}$$

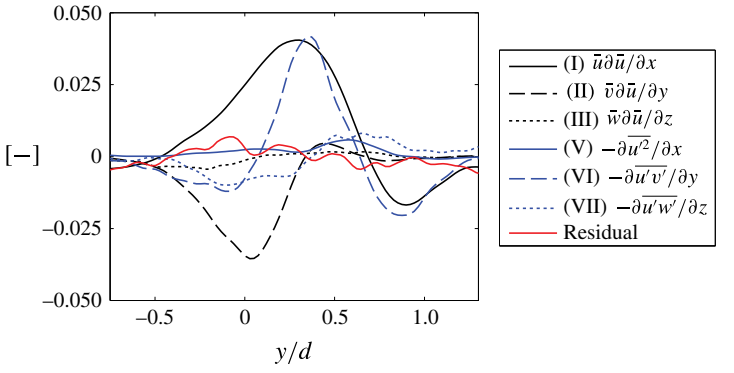

FIGURE 11. Lateral profiles of the terms of the x-RANS equation (3.6) at $x/d = 6$ for $\gamma = 30°$ and $\lambda = \lambda_o$. Profiles are non-dimensionalized with $\bar{u}_h^2$ and d.

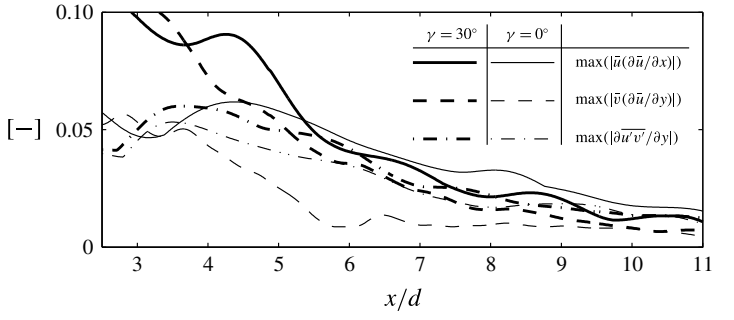

FIGURE 12. Variation of the maximum values of the dominant terms of the x-RANS equation (3.6) at hub height as a function of the downwind distance for two different yaw angles ($\gamma = 0°$ and 30°) at $\lambda = \lambda_o$. Profiles are non-dimensionalized with $\bar{u}_h^2$ and d.

As shown in figures 9 and 11, the first term on the right-hand side of the equation is negligible compared to the other terms. Moreover, $\overline{u'v'}$ and $\overline{u'w'}$ in the second and third terms on the right-hand side can be modelled with $-\nu_T(\partial\bar{u}/\partial y)$ and $-\nu_T(\partial\bar{u}/\partial z)$, respectively, where ν_T is the turbulent viscosity. The left-hand side can also be rearranged based on the quotient derivative rule, which yields

$$\frac{\partial(\bar{v}/\bar{u})}{\partial y} + \frac{\partial(\bar{w}/\bar{u})}{\partial z} = -\frac{\nu_T}{\bar{u}^2}\frac{\partial^2\bar{u}}{\partial y^2} - \frac{\nu_T}{\bar{u}^2}\frac{\partial^2\bar{u}}{\partial z^2}. \tag{3.8}$$

$\bar{v}/\bar{u}$ in the above equation is equal to $\arctan\theta$, where θ denotes the wake skew angle with respect to the streamwise direction. Our wind tunnel measurements as well as LES data (Jiménez *et al.* 2010) show that θ is always small even in extreme conditions (much smaller than 10° even at $\gamma = 30°$ and $C_T = 0.8$), so $\tan\theta \approx \theta$ and $\bar{v}/\bar{u}$ can be replaced with θ in (3.8). The above equation can be therefore written as

$$\frac{\partial\theta}{\partial y} + \frac{\partial(\bar{w}/\bar{u})}{\partial z} = -\frac{\nu_T}{\bar{u}^2}\frac{\partial^2\bar{u}}{\partial y^2} - \frac{\nu_T}{\bar{u}^2}\frac{\partial^2\bar{u}}{\partial z^2}. \tag{3.9}$$

In appendix A, (3.9) is employed to mathematically prove that $\partial\bar{u}/\partial y$ has an extremum (i.e. $\partial^2\bar{u}/\partial y^2 = 0$) if the skew angle has an extremum (i.e. $\partial\theta/\partial y = 0$). The proof

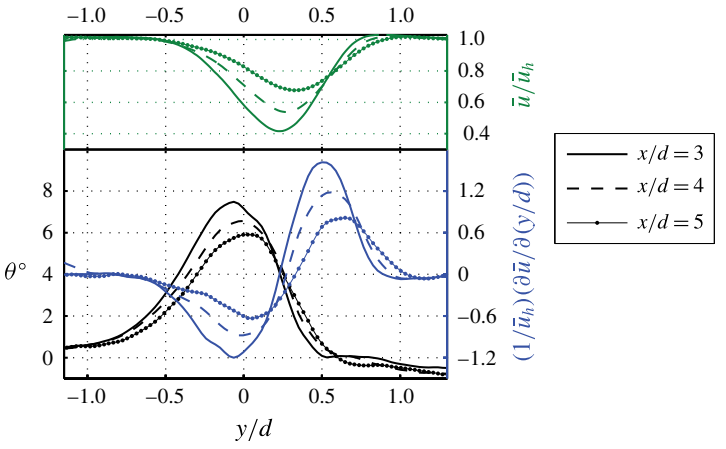

FIGURE 13. Variation of θ, $(1/\bar{u}_h)(\partial\bar{u}/\partial(y/d))$ and $(\bar{u}/\bar{u}_h)$ in the spanwise direction at three different downwind positions ($x/d = 3$, 4, and 5) for a turbine with $\gamma = 30°$ and $\lambda = \lambda_o$.

is provided for the wake of a turbine with a low yaw angle and a uniform inflow. However, figure 13 shows that this finding is in good agreement with the PIV data even for the turbine wake with $\gamma = 30°$ in boundary-layer inflow conditions. In fact, it can be seen in the figure that the maximum value of θ is in one side of the wake rather than the wake centre, and it exactly occurs where $\partial^2\bar{u}/\partial y^2 = 0$. It seems that there is another extremum for θ profiles on the other side of the wake where $\partial^2\bar{u}/\partial y^2 = 0$ but it is difficult to comment on that as the magnitude of θ is very small on that side. It is worth mentioning that this finding, purely based on the x-RANS and continuity equations, is likely to be valid for other similar free shear flows such as inclined jets in cross-flow.

This asymmetric distribution of the skew angle with respect to the wake centre can also provide more insight on the origin of the wake deflection for yawed turbines. As shown in figure 11, terms (I), (II) and (VI) are the dominant terms of (3.6) at hub height in the far wake of a yawed turbine. They can be readily rewritten as

$$\frac{\partial\bar{u}}{\partial x} \approx \frac{\nu_T}{\bar{u}}\frac{\partial^2\bar{u}}{\partial y^2} - \theta\frac{\partial\bar{u}}{\partial y}. \tag{3.10}$$

The first term on the right-hand side of (3.10) is approximately symmetric with respect to the wake centre. The maximum value of the second term on the right-hand side, however, occurs where θ is maximum (see figure 13). As a result, the term on the left-hand side of (3.10), $\partial\bar{u}/\partial x$, has to be asymmetric with respect to the wake centre so that the equation remains balanced. This implies that the wake velocity recovers faster on the side of the wake in which θ is bigger and, as a consequence, the wake shifts to the opposite side as it moves downstream. In other words, the wake deflection for yawed turbines cannot occur unless θ has an asymmetric distribution with respect to the wake centre.

The RANS equation in the spanwise direction at high Reynolds numbers is

$$\underbrace{\bar{u}\frac{\partial\bar{v}}{\partial x}}_{\text{(I)}} + \underbrace{\bar{v}\frac{\partial\bar{v}}{\partial y}}_{\text{(II)}} + \underbrace{\bar{w}\frac{\partial\bar{v}}{\partial z}}_{\text{(III)}} = -\underbrace{\frac{1}{\rho}\frac{\partial\bar{p}}{\partial y}}_{\text{(IV)}} - \underbrace{\frac{\partial\overline{u'v'}}{\partial x}}_{\text{(V)}} - \underbrace{\frac{\partial\overline{v'^2}}{\partial y}}_{\text{(VI)}} - \underbrace{\frac{\partial\overline{v'w'}}{\partial z}}_{\text{(VII)}}. \tag{3.11}$$

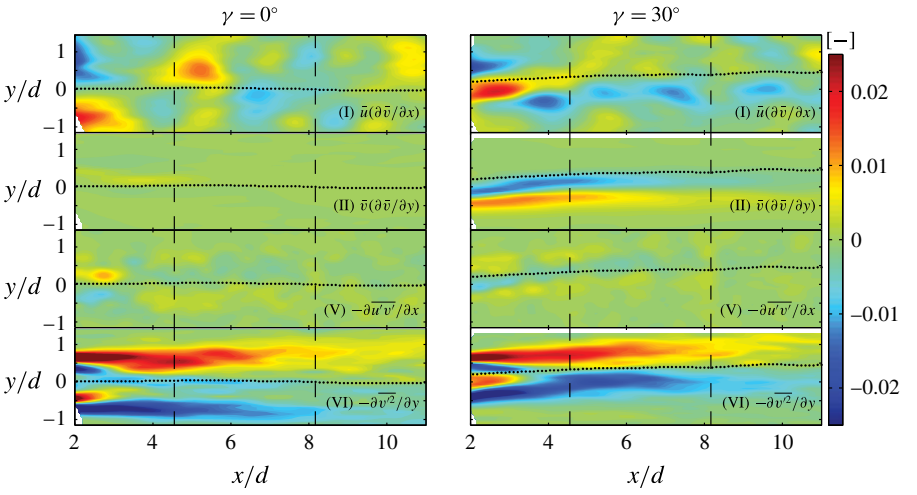

FIGURE 14. Contours of the terms of the y-RANS equation (3.11) measured in the horizontal plane at hub height for two different yaw angles ($\gamma = 0°$ and $30°$) at $\lambda = \lambda_o$. Contours are non-dimensionalized with $\bar{u}_h^2$ and d. Black dots represent the locus of the maximum velocity deficit in the measured plane, and overlapped locations of PIV planes are indicated by vertical dashed lines.

Contours of the terms of (3.11) measured in the horizontal plane are shown in figure 14. In addition, contours of the terms of (3.11) measured in a yz plane at $x/d = 6$ are shown in figure 15. It can be seen that $\partial\overline{v'^2}/\partial y$ is generally bigger than the other terms, particularly in the far-wake region. This term is likely to be balanced with the pressure gradient term (term (IV)) which is the only term of (3.11) not measured in the present work. Note that these two terms are also in balance in the two-dimensional boundary-layer form of RANS equations (Pope 2000).

3.3. *Integral form of RANS equations*

The integral form of the RANS equation in the streamwise direction has been extensively used in classical studies of bluff-body wakes (see Tennekes & Lumley 1972; Pope 2000; Johansson, George & Gourlay 2003). As the mean incoming velocity $\bar{u}_\infty$ is only a function of z, equation (3.6), after neglecting the pressure term, can be written as

$$\bar{u}\frac{\partial(\bar{u}_\infty - \bar{u})}{\partial x} + \bar{v}\frac{\partial(\bar{u}_\infty - \bar{u})}{\partial y} + \bar{w}\frac{\partial(\bar{u}_\infty - \bar{u})}{\partial z} = \frac{\partial\overline{u'^2}}{\partial x} + \frac{\partial\overline{u'v'}}{\partial y} + \frac{\partial\overline{u'w'}}{\partial z} + \bar{w}\frac{\mathrm{d}\bar{u}_\infty}{\mathrm{d}z}. \quad (3.12)$$

Equation (3.12) can also be written in conservative form. In order to do that, we multiply the continuity equation (3.1) by $(\bar{u}_\infty - \bar{u})$ and then add the resultant equation to the left-hand side of (3.12). We obtain

$$\frac{\partial\bar{u}(\bar{u}_\infty - \bar{u})}{\partial x} + \frac{\partial\bar{v}(\bar{u}_\infty - \bar{u})}{\partial y} + \frac{\partial\bar{w}(\bar{u}_\infty - \bar{u})}{\partial z} = \frac{\partial\overline{u'^2}}{\partial x} + \frac{\partial\overline{u'v'}}{\partial y} + \frac{\partial\overline{u'w'}}{\partial z} + \bar{w}\frac{\mathrm{d}\bar{u}_\infty}{\mathrm{d}z}. \quad (3.13)$$

In order to integrate (3.13) with respect to y and z from $-\infty$ to ∞, we neglect the presence of the ground. Note that, however, this assumption might be questionable

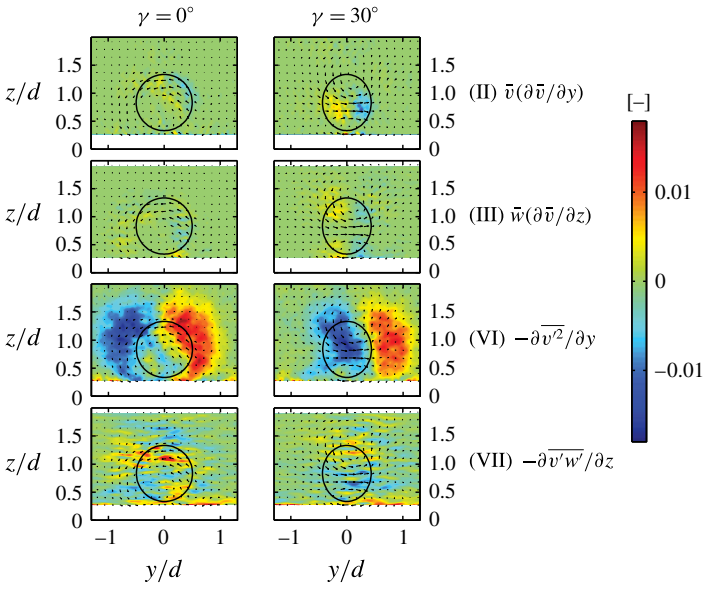

FIGURE 15. Contours of the terms of the y-RANS equation (3.11) measured in a yz plane at $x/d = 6$ for two different yaw angles ($\gamma = 0°$ and $30°$) at $\lambda = \lambda_o$. Contours are non-dimensionalized with $\bar{u}_h^2$ and d. Black circles indicate the frontal area of the wind turbine. The vector field represents the in-plane velocity components.

for very far-wake regions, where the wake clearly hits the ground. Integrating (3.13) leads to

$$\left(\frac{\mathrm{d}}{\mathrm{d}x}\int_{-\infty}^{\infty}\int_{-\infty}^{\infty}[\bar{u}(\bar{u}_\infty - \bar{u}) - \overline{u'^2}]\,\mathrm{d}y\,\mathrm{d}z\right) - \int_{-\infty}^{\infty}\int_{-\infty}^{\infty}\bar{w}\frac{\mathrm{d}\bar{u}_\infty}{\mathrm{d}z}\,\mathrm{d}y\,\mathrm{d}z = 0. \tag{3.14}$$

The last term of the above equation can be neglected if: (i) the velocity gradient $\mathrm{d}\bar{u}_\infty/\mathrm{d}z$ of the incoming boundary layer is not very large and (ii) the yaw angle is not very high. Note that from the discussion of § 3.1, $\bar{w}$ is much smaller than the streamwise velocity deficit in the far-wake region for low yaw angles. Additionally, as shown in figure 9, the variation of $\overline{u'^2}$ in the streamwise direction is considerably smaller than the streamwise convective term, so it can be neglected in (3.14). Thus, (3.14) can be approximated as

$$\frac{\mathrm{d}}{\mathrm{d}x}\int_{-\infty}^{\infty}\int_{-\infty}^{\infty}[\bar{u}(\bar{u}_\infty - \bar{u})]\,\mathrm{d}y\,\mathrm{d}z \approx 0. \tag{3.15}$$

This well-known equation states that the streamwise momentum deficit flow rate is conserved and independent of the downwind location.

To predict the wake deflection for a yawed turbine, we also need the integral form of the RANS equation in the spanwise direction. Multiplying the continuity equation (3.1) by $\bar{v}$ and then adding the resultant equation to the left-hand side of (3.11) leads to

$$\frac{\partial\bar{u}\bar{v}}{\partial x} + \frac{\partial\bar{v}\bar{v}}{\partial y} + \frac{\partial\bar{w}\bar{v}}{\partial z} = -\frac{1}{\rho}\frac{\partial\bar{p}}{\partial y} - \frac{\partial\overline{u'v'}}{\partial x} - \frac{\partial\overline{v'^2}}{\partial y} - \frac{\partial\overline{v'w'}}{\partial z}. \tag{3.16}$$

Integrating with respect to y and z from $-\infty$ to ∞, we obtain

$$\frac{\mathrm{d}}{\mathrm{d}x}\int_{-\infty}^{\infty}\int_{-\infty}^{\infty}(\bar{u}\bar{v}+\overline{u'v'})\,\mathrm{d}y\,\mathrm{d}z=0. \tag{3.17}$$

It is interesting to note that both dominant terms of the differential form of the spanwise momentum equation (terms (IV) and (VI) in (3.11)) are eliminated in its integral form (3.17). As no specific assumption is made to develop (3.17), it can be used for similar type of flows such as the wakes of airfoils or inclined jets in cross-flow. To our knowledge, our work is the first study that analyses the budget of RANS equations in both streamwise and spanwise directions for a turbine wake, and also develops the integral form of RANS equation in the spanwise direction. Equation (3.17) can be simplified since the shear stress term is generally smaller than the advection term for a yawed turbine (see figure 14). $\bar{v}$ can be also replaced with $\bar{u}\theta$, hence

$$\frac{\mathrm{d}}{\mathrm{d}x}\int_{-\infty}^{\infty}\int_{-\infty}^{\infty}\bar{u}^2\theta\,\mathrm{d}y\,\mathrm{d}z\approx 0. \tag{3.18}$$

The above equation states that the flow rate of spanwise momentum is conserved, regardless of the downwind location.

4. Self-similarity

It is well known that bluff-body wakes achieve self-similarity at a certain downwind distance. This means that the velocity deficit $\Delta\bar{u}$ profiles normalized by the maximum velocity deficit $\Delta\bar{u}_c$ against y^*/σ collapse onto a single curve for different downwind locations (Tennekes & Lumley 1972), where σ is the characteristic width of the wake and y^* is the lateral distance from the wake centre. Different possible ways were introduced in the literature to define the characteristic width of the wake: (i) the wake half-width $r_{1/2}$, where the velocity deficit is half of its maximum value (Pope 2000), (ii) the position where the velocity is 99 % of the incoming velocity and (iii) the standard deviation of a Gaussian fit of the velocity-deficit profile (Bastankhah & Porté-Agel 2014). The first two methods are rather sensitive to the measurement uncertainty and the latter only works accurately for purely Gaussian profiles. If spatially resolved wake velocity profiles (e.g. from LES or PIV data) are available, the below equation does not have the mentioned limitations, and it can provide a more robust definition for the wake width:

$$\sigma_y=\frac{1}{\sqrt{2\pi}(\bar{u}_\infty-\bar{u}_c)}\lim_{y\to\infty}\int_{-y}^{y}(\bar{u}_\infty-\bar{u})\,\mathrm{d}\hat{y}, \tag{4.1}$$

where σ_y is the wake width in y direction, $\bar{u}_c$ is the velocity of the wake centre and $\hat{y}$ is the integration variable. The integral can be calculated numerically to find the wake width at each downstream position. An equation similar to (4.1) can be also written for the wake width in the vertical direction. Note that for a pure Gaussian profile, (4.1) reduces to the standard deviation of the profile.

Previous studies showed that the velocity profiles in turbine wakes with zero yaw become self-similar rather quickly (Bastankhah & Porté-Agel 2014; Abkar & Porté-Agel 2015; Xie & Archer 2015). Figure 16(*a*) shows the lateral profiles of the normalized velocity deficit for the wake of a yawed turbine. As seen in the figure, despite the wake deflection, the wake of yawed turbines exhibits some degree of

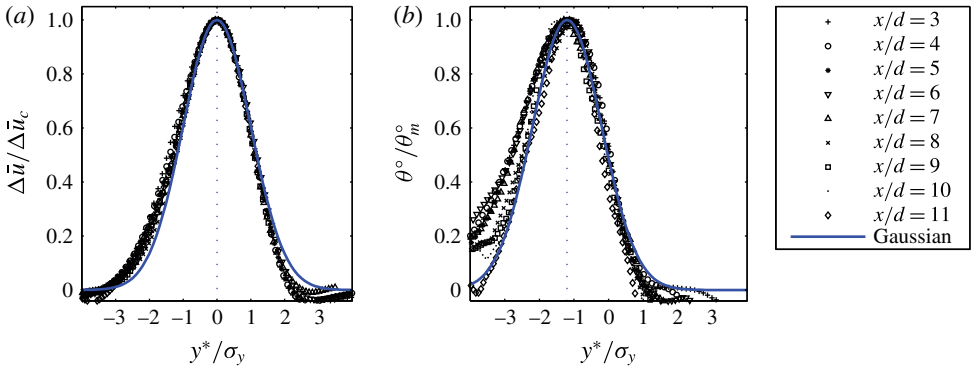

FIGURE 16. The self-similar lateral profiles of (*a*) velocity deficit, and (*b*) wake skew angle at different downwind positions in the wake of a turbine with $\gamma = 30^\circ$ and $\lambda = \lambda_o$.

self-similarity in the horizontal plane at hub height. As mentioned earlier, one side of the wake (the left side in figure 16*a*) is influenced by the strong spanwise velocity distribution which makes the wake velocity profile slightly skewed and, as a result, the degree of self-similarity is inferior in this side. However, the figure shows that in general self-similarity can be assumed for lateral velocity profiles in the far-wake region. Additionally, akin to bluff-body wakes, a Gaussian distribution, written as

$$\frac{\Delta\bar{u}}{\Delta\bar{u}_c} = \mathrm{e}^{-0.5(y_*/\sigma_y)^2}, \tag{4.2}$$

acceptably fits the self-similar velocity profiles for most of the wake except the edges. In addition to the velocity profiles, the lateral profiles of the wake skew angle θ exhibit self-similarity to some extent, as shown by figure 16(*b*). Although the collapse of the θ-profiles is not as remarkable as the one for the velocity profiles, the figure shows that a Gaussian curve can be still used to approximately express the variation of θ. The centre of the fitted Gaussian curve for θ profiles, however, lies somewhere close to $y^* = -\sigma_y$. Note that the peak value of θ should be located exactly at $y^* = -\sigma_y$ for a pure Gaussian velocity profile given the fact that at this lateral position $\partial^2\bar{u}/\partial y^2 = 0$, and θ is thus maximum according to (3.9) and confirmed in figure 13. This small difference seen in the figure is due to the moderately asymmetric distribution of the velocity profiles discussed earlier. The wake skew angle distribution in the y direction can be therefore approximated by

$$\frac{\theta}{\theta_m} = \mathrm{e}^{-0.5(y_*/\sigma_y+1)^2}, \tag{4.3}$$

where θ_m is the maximum skew angle at each downwind location.

The value of the wake width at each downstream position is very important as it is used to examine self-similarity. Furthermore, the proper estimation of its variation with the downwind distance is critical for the accurate prediction of the wake velocity distribution. In the absence of ambient turbulence, classical theories of free shear flows (see Tennekes & Lumley 1972; Pope 2000) state the well-known fact that three-dimensional turbulent wakes of bluff bodies such as disks and spheres grow proportional to $x^{-1/3}$, and the velocity deficit decays with x as $x^{-2/3}$. Far wakes

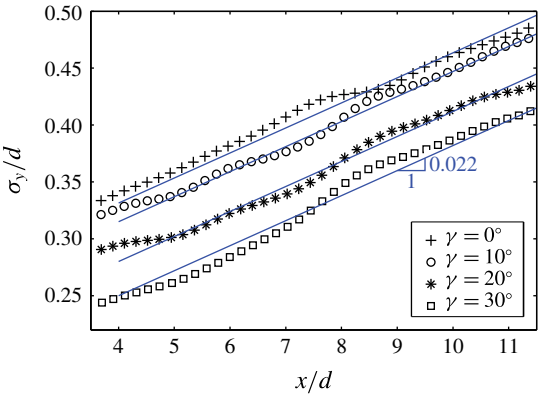

FIGURE 17. Variation of the normalized lateral wake width σ_y/d for $\lambda = \lambda_o$: $\gamma = 0°$ (plus), $\gamma = 10°$ (circle), $\gamma = 20°$ (asterisk), $\gamma = 30°$ (square). Fitted lines with the slope of 0.022 are shown by blue lines.

of wind turbines are also shown to behave similarly under laminar inflow conditions (Dufresne & Wosnik 2013; Okulov *et al.* 2015). The evolution of wake flows is, however, considerably modified in the case of turbulent inflow conditions (Wu & Faeth 1994; Bagchi & Balachandar 2004; Amoura *et al.* 2010). Different numerical and experimental studies on wakes of spheres (e.g. Legendre, Merle & Magnaudet 2006), cylinders (e.g. Eames, Jonsson & Johnson 2011*b*) and wind turbines (see Bastankhah & Porté-Agel 2014; Johnson *et al.* 2014) showed that turbulent far wakes grow approximately linearly with x in the presence of ambient turbulence. Eames *et al.* (2011*a*) tried to mathematically model the interaction of the ambient turbulence with wake flows. They suggested that the wake grows linearly with x and the wake growth rate is proportional to the incoming streamwise turbulence intensity provided that: (i) the velocity deficit is comparable or smaller than the standard deviation of the incoming velocity and (ii) the wake radius is not bigger than the integral length scale of the incoming flow. In turbulent boundary-layer flows, both of these conditions are expected to be fulfilled for a broad streamwise range in turbine far wakes.

Figure 17 shows the wake width variation with the downwind distance calculated by (4.1) for different yaw angles. It can be seen that the wake width varies approximately linearly in the far-wake region for different yaw angles which is consistent with previous studies as the incoming flow is turbulent. In addition, the figure shows notably that the wake growth rate k is approximately the same for all the different yaw angles ($k = 0.022$ for this experimental configuration). This is in contrast with the common conjecture stating that the wake growth rate increases with increase in yaw angle (Jiménez *et al.* 2010). This can be explained by the fact that, as discussed in § 3.2, the wake of a yawed turbine quickly asymptotes to a turbulent free shear flow in the far-wake region. In this flow regime, the wake recovery is mainly influenced by the incoming flow properties such as the ambient turbulence (Vermeulen 1980). Turbine characteristics such as the thrust coefficient C_T or the yaw angle γ are likely to only affect the wake characteristics in the onset of the far-wake region. See for instance the intercepts of parallel lines corresponding to different yaw angles in figure 17. In the current study, the incoming turbulent boundary layer remained unchanged during the measurements, so the wake growth rate k is expected to be the same for different yaw angles.

5. Model derivation for the far-wake region

It is shown in § 4 that velocity-deficit and skew angle profiles in the y direction can be acceptably represented by self-similar Gaussian distributions even for high yaw angles. However, a Gaussian profile cannot be fitted satisfactorily to the profiles in the z direction for turbines with high yaw angles (e.g. $\gamma = 30°$) since the wake cross-section has a kidney shape due to the presence of the CVP, as discussed in detail in § 3.1 and shown in figure 5. Therefore, one may consider a more complicated shape in the z direction for this case, e.g. a bimodel distribution as used by Kikkert (2006) to represent the cross-section of cross-flow jets. However, yaw angles greater and equal to 30° are rather impractical for yaw-angle control methods, which is our main motivation to derive a simple analytical model for wind turbine wakes in yawed conditions. This is due to the fact that the substantial reduction in turbine power caused by a yaw angle of 30° is unlikely to be compensated by the increase in the power of downwind turbines (Jiménez *et al.* 2010).

As seen in our PIV measurements of turbine wakes as well as flow visualizations of inclined jets in cross-flow (Wang & Kikkert 2014), the presence of the CVP is not strong for angles smaller than 30°, so a Gaussian distribution may still be used to approximate the wake in the z direction for yaw angles smaller than 30°. As a result, it seems unnecessary to consider a more complicated profile in the z direction, and a Gaussian distribution in both the y and z directions is used in this paper to approximate the velocity and skew angle profiles. It is worth mentioning that similar distribution has been also extensively used in studies of cross-flow jets (e.g. Fan 1967; Abraham 1970; Ooms 1972) due to its simplicity. The velocity and skew angle distribution in the wake of a yawed turbine can be therefore written as

$$\left.\begin{aligned} \frac{\bar{u}(x,y,z)}{\bar{u}_\infty} &= 1 - C\mathrm{e}^{-(y-\delta)^2/2\sigma_y^2}\mathrm{e}^{-(z-z_h)^2/2\sigma_z^2}, \\ \frac{\theta(x,y,z)}{\theta_m} &= \mathrm{e}^{-(y-\delta+\sigma_y)^2/2\sigma_y^2}\mathrm{e}^{-(z-z_h)^2/2\sigma_z^2}, \end{aligned}\right\} \tag{5.1}$$

where C is the velocity deficit at the wake centre normalized with the incoming velocity (i.e. $\Delta\bar{u}_c/\bar{u}_\infty$) and δ is the wake-centre deflection at each downwind location. The wake centre in (5.1) is assumed to remain at hub height z_h as the vertical displacement of the wake centre is rather small for lower yaw angles (see figure 5). Furthermore, different wake widths in the y and z directions are considered in (5.1), denoted by σ_y and σ_z, respectively. Previous studies showed that the wake of a non-yawed turbine might have different widths in the spanwise and vertical directions due to the effect of ground (Xie & Archer 2015) or incoming boundary-layer conditions (Abkar & Porté-Agel 2015). The difference is, however, inevitable and more significant for a yawed turbine as its frontal area is an ellipse, instead of a circle, with the minor axis equal to $d\cos\gamma$ in the spanwise direction and the major axis equal to d in the vertical direction.

Substituting $\bar{u}$ in (3.15) with (5.1) and integrating results in

$$\pi\bar{u}_\infty^2\frac{\mathrm{d}}{\mathrm{d}x}[\sigma_y\sigma_z C(2-C)] = 0. \tag{5.2}$$

The above equation is valid only in the far-wake region where the velocity distribution can be expressed by (5.1). In other words, (5.2) can be used from $x = x_0$ to ∞,

where x_0 indicates the downwind location where the velocity distribution achieves self-similarity. Thus, (5.2) can be written as

$$\sigma_{y_0}\sigma_{z_0}C_0(2-C_0)=\sigma_y\sigma_z C(2-C). \tag{5.3}$$

The values of variables at $x=x_0$ are shown with a zero in the subscript in (5.3) and in the remainder of this paper. All the variables related to $x=x_0$ will be determined in § 6. For now, they are assumed as known values. Solving (5.3) for C gives

$$C=1-\sqrt{1-\frac{(\sigma_{y_0}\sigma_{z_0})M_0}{(\sigma_y\sigma_z)}}, \tag{5.4}$$

where $M_0 = C_0(2 - C_0)$. Equation (5.4) gives the maximum velocity deficit as a function of wake conditions in the far-wake onset (σ_{y_0}, σ_{z_0} and M_0) and wake widths (σ_y and σ_z). It is already seen in § 4 that turbine far wakes expands approximately linearly with x in our interested streamwise range under the boundary-layer inflow condition which is always the case for wind turbines operating in the field. Therefore, σ_y and σ_z can be estimated by

$$\left.\begin{aligned}\frac{\sigma_y}{d}&=k_y\frac{(x-x_0)}{d}+\sigma_{y_0},\\ \frac{\sigma_z}{d}&=k_z\frac{(x-x_0)}{d}+\sigma_{z_0},\end{aligned}\right\} \tag{5.5}$$

where k_y and k_z are the wake growth rates in the spanwise and vertical directions, respectively.

Next, the wake deflection in the far-wake region will be determined. Inserting (5.1) in (3.18) and then integrating yields

$$\frac{2\pi\bar{u}_\infty^2}{3\mathrm{e}^{1/3}}\frac{\mathrm{d}}{\mathrm{d}x}[\theta_m\sigma_y\sigma_z(C^2-3\mathrm{e}^{1/12}C+3\mathrm{e}^{1/3})]=0, \tag{5.6}$$

so the wake skew angle of the wake centre θ_c ($\theta_c=\theta_m\mathrm{e}^{-0.5}$) can be written as

$$\theta_c=\frac{\theta_{c_0}(\sigma_{y_0}\sigma_{z_0})E_0}{\sigma_y\sigma_z(C^2-3\mathrm{e}^{1/12}C+3\mathrm{e}^{1/3})}, \tag{5.7}$$

where $E_0=C_0^2-3\mathrm{e}^{1/12}C_0+3\mathrm{e}^{1/3}$. Equation (5.7) can be integrated to find the wake deflection. After some algebraic manipulations (see appendix B), δ can be written as

$$\delta=\delta_0+\frac{\theta_{c_0}E_0}{5.2}\sqrt{\frac{\sigma_{y_0}\sigma_{z_0}}{k_yk_zM_0}}\ln\left[\frac{(1.6+\sqrt{M_0})\left(1.6\sqrt{\frac{\sigma_y\sigma_z}{\sigma_{y_0}\sigma_{z_0}}}-\sqrt{M_0}\right)}{(1.6-\sqrt{M_0})\left(1.6\sqrt{\frac{\sigma_y\sigma_z}{\sigma_{y_0}\sigma_{z_0}}}+\sqrt{M_0}\right)}\right]. \tag{5.8}$$

Equation (5.8) gives the value of the wake deflection δ at each downwind location as a function of the wake characteristics in the far-wake onset as well as the wake growth rate. Note that (5.8) only takes into account the wake deflection due to yawing of the turbine, and the slight horizontal deflection caused by the interaction of the rotating wake and the incoming shear flow reported by Fleming *et al.* (2014) is not considered in the current study.

To close the model, the wake characteristics in the onset of the far-wake region (i.e. the values of variables at $x = x_0$) should be determined. The values of C_0, θ_{c_0}, σ_{y_0}, σ_{z_0} and δ_0 will therefore be specified in § 6.

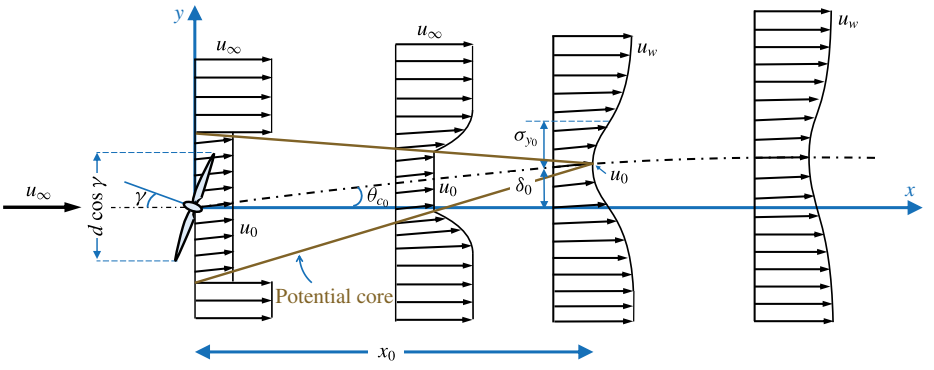

FIGURE 18. Schematic of the wake of a yawed turbine.

6. Onset of the far-wake region

To find the wake characteristics in the onset of the far-wake region, one can benefit from the analogy between wakes and coflowing jets. For a jet in coflow, a region with a uniform velocity, called potential core, develops after the jet exit. The potential core, however, diminishes gradually as it moves downstream due to its interaction with the surroundings (Rajaratnam 1976). After a certain downwind distance, the potential core ultimately disappears and the velocity profile develops fully into a self-similar Gaussian distribution (Fan 1967). Few early studies (e.g. Lissaman 1979; Vermeulen 1980) tried to model the near wake of a non-yawed turbine in a similar manner. Although this idealized image of the near wake cannot evidently predict the detailed characteristics of this complex region, it will be shown in the following that it can be used to provide key characteristics of the far-wake onset, which are needed to model the far-wake region.

Figure 18 shows an idealized schematic of the wake of a yawed turbine. As the wake moves downstream, the potential core becomes smaller until it eventually ends at $x = x_0$. Before reaching this point, however, the central part of the potential core is not influenced by the ambient flow. Accordingly, the flow angle and the velocity magnitude in the wake centre do not change across the potential core. After the termination of the potential core, the recovery of the wake centre starts, and the wake deflection angle decreases due to the interaction with the ambient flow. The velocity and the wake deflection angle in the potential core are denoted by u_0 and θ_{c_0}, respectively, in figure 18.

As mentioned in § 1, extensive research has been performed on yawed rotors and the flow passing through them mainly to improve the performance of helicopters and autogiros. Different methods have been suggested in the literature to relate C_T of yawed rotors to the induction factor in the direction normal to the rotor denoted by a. The one suggested by Glauert (1926) is widely used in previous studies (e.g. Sant 2007; Haans 2011) as it is simple and also able to estimate the thrust force of yawed turbines correctly (Burton *et al.* 1995). A more complicated alternative model is the one obtained with the vortex theory (see Burton *et al.* (1995) for the detailed discussion). However, both predict rather similar variation of C_T as a function of a, especially for $\gamma \leqslant 20°$. Thus, the former one is used in the current study for the sake of simplicity. Based on this model, the thrust coefficient C_T of a yawed rotor is determined by

$$C_T = \frac{4au_R}{u_\infty} = 4a\sqrt{1 - a(2\cos\gamma - a)}, \tag{6.1}$$

where u_R is the wind velocity at the rotor. Since we need to know the value of the normal induction factor a for a given C_T, the current form of (6.1) is not suitable because it has to be solved numerically for each value of C_T. Alternatively, an approximate expression of a can be found from (6.1) as seen in the following. First, (6.1) can be simplified as in general $\sqrt{1-x}$ asymptotes to $(1-0.5x)$ for small values of x. Moreover, a can be ignored compared to $2\cos\gamma$, especially for lower yaw angles. Hence,

$$C_T \approx 4a(1 - a\cos\gamma). \tag{6.2}$$

From (6.2), we obtain

$$a \approx \frac{1}{2\cos\gamma}(1 - \sqrt{1 - C_T\cos\gamma}). \tag{6.3}$$

The value of a predicted by (6.3) always lies within $\pm 5\,\%$ of the true value provided that $C_T \leqslant 1$ and $\gamma \leqslant 30^\circ$. Substituting (6.3) into (6.1) gives u_R as a function of C_T and γ:

$$\frac{u_R}{u_\infty} = \frac{C_T\cos\gamma}{2(1 - \sqrt{1 - C_T\cos\gamma})}. \tag{6.4}$$

The pressure of the air drops as it passes through the rotor; however, it returns to atmospheric pressure shortly downstream. Based on Bernoulli's equation, the velocity further decreases from u_R to u_0 (Sørensen 2015). Applying the Bernoulli's equation in both upwind and downwind sides of the rotor results in

$$\text{upwind} \quad p_\infty + \tfrac{1}{2}\rho u_\infty^2 = p_R^+ + \tfrac{1}{2}\rho u_R^2, \tag{6.5}$$

$$\text{downwind} \quad p_R^- + \tfrac{1}{2}\rho u_R^2 = p_\infty + \tfrac{1}{2}\rho u_0^2, \tag{6.6}$$

where p_R^+ and p_R^- are the air pressure in front and back of the rotor, respectively. Subtracting the two equations to obtain the pressure drop across the rotor and then replacing the pressure drop with $(1/2)\rho u_\infty^2 C_T$ give the following simple relationship for u_0:

$$\frac{u_0}{u_\infty} = \sqrt{1 - C_T}. \tag{6.7}$$

Note that u_0, unlike u_R, depends only on C_T for any yaw angle. The distance from the rotor to where the air velocity becomes equal to u_0 is typically assumed to be very small (Frandsen *et al.* 2006), so for the sake of simplicity, we assume that the air velocity remains equal to u_0 from $x = 0$ to x_0 across the whole potential core (see figure 18).

Figure 19 shows experimental values of the normalized maximum velocity deficit in the horizontal plane at hub height for different yaw angles and tip-speed ratios. In addition, the theoretical value of the normalized velocity deficit in the potential core (i.e. $C_0 = 1 - u_0/u_\infty$) predicted by (6.7) is shown in the figure by horizontal blue lines. As seen in the figure, not only are the real values of the maximum velocity deficit in all cases higher than the theoretical ones, but also they are not constant in the near-wake region in contrast with the assumption of constant velocity for the potential core. This departure is expected as the near-wake region has a highly complex structure due to the effect of the nacelle, rotating blades, etc. so we are unable to predict detailed characteristics of the near-wake region by assuming a potential core downwind of the turbine. However, it will be shown later that it can be still quite useful to provide some general but essential information about the

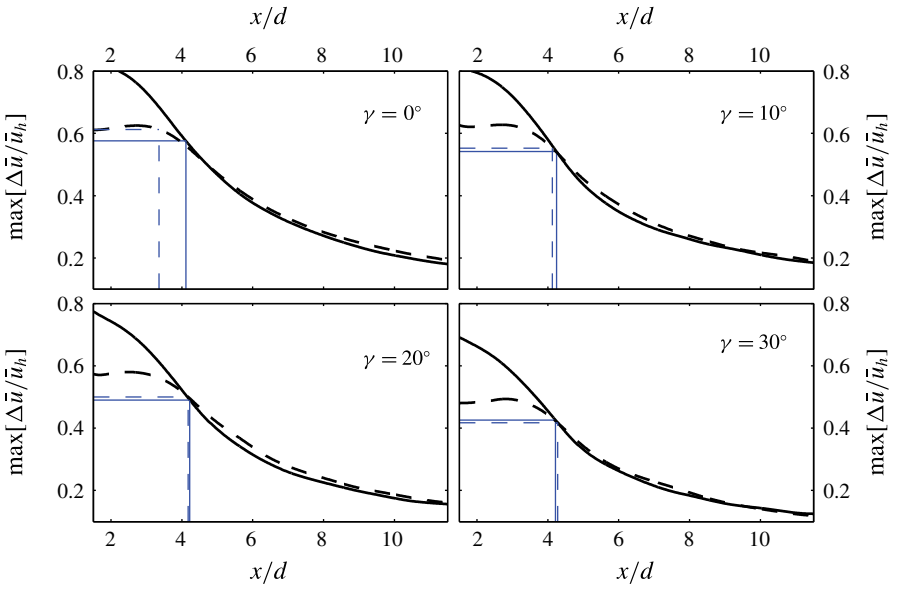

FIGURE 19. Variation of the maximum normalized wake velocity deficit in the horizontal plane at hub height for different yaw angles shown by black lines. Solid lines and dashed lines correspond to $\lambda = \lambda_o$ and λ_f, respectively. Horizontal and vertical blue lines represent the values of u_0 and x_0 for each case, respectively.

near-wake region. As already implemented by Vermeulen (1980) for a non-yawed turbine, the location where the velocity deficit at the wake centre reaches to the theoretical value can be considered as the end of the potential core (i.e. $x = x_0$) which is shown by vertical blue lines in figure 19.

It is important to note that as u_0 is smaller than u_R, the potential core area at $x = 0$ should be considered bigger than the rotor area so that the mass is conserved. Based on mass conservation, the potential core area at $x = 0$ is an ellipse whose vertical major axis is $d\sqrt{u_R/u_0}$ and lateral minor axis is equal to $d\cos\gamma\sqrt{u_R/u_0}$. It is worth remembering that the frontal rotor area is an ellipse with major and minor axes of d and $d\cos\gamma$, respectively.

As mentioned in § 3.2, the streamwise momentum deficit flow rate is almost constant along the streamwise direction (3.15). Given the velocity distribution at $x = 0$ and x_0, the value of the streamwise momentum deficit flow rate can be calculated for these two locations as follows:

$$\int_{-\infty}^{\infty}\int_{-\infty}^{\infty}[u(u_\infty - u)]\,\mathrm{d}y\,\mathrm{d}z = \begin{cases} \dfrac{\pi d^2}{4}\dfrac{u_R}{u_0}\cos\gamma\, u_0(u_\infty - u_0) & \text{at } x = 0 \\ \pi\sigma_{y_0}\sigma_{z_0}(u_\infty + u_0)(u_\infty - u_0) & \text{at } x = x_0. \end{cases} \tag{6.8}$$

Equating the two equations, and assuming an elliptic wake cross-section imposed by the rotor frontal area results in

$$\frac{\sigma_{z_0}}{d} = \frac{1}{2}\sqrt{\frac{u_R}{u_\infty + u_0}}, \quad \frac{\sigma_{y_0}}{d} = \frac{\sigma_{z_0}}{d}\cos\gamma. \tag{6.9a,b}$$

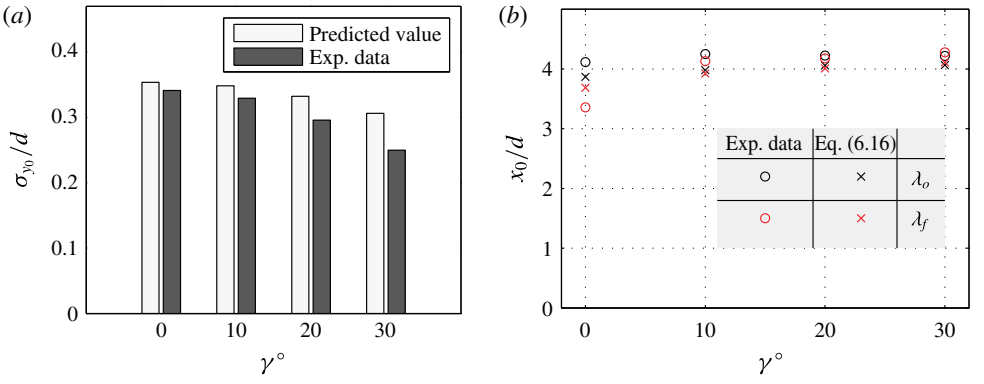

FIGURE 20. (*a*) The value of the normalised lateral wake width at $x = x_0$, σ_{y_0}/d, for different yaw angles. The light grey bars show the values predicted by (6.10), and the black ones show the experimental data. (*b*) The prediction of the normalized potential core length x_0/d compared with the experimental data for different yaw angles and tip-speed ratios.

Inserting (6.4) and (6.7) into (6.9) leads to

$$\left.\begin{aligned} \frac{\sigma_{z_0}}{d} &= \sqrt{\frac{1+\sqrt{1-C_T\cos\gamma}}{8(1+\sqrt{1-C_T})}} \approx \sqrt{\frac{1}{8}}, \\ \frac{\sigma_{y_0}}{d} &= \frac{\sigma_{z_0}}{d}\cos\gamma. \end{aligned}\right\} \tag{6.10}$$

It is interesting to note that for a zero yawed turbine, σ_{y_0}/d and σ_{z_0}/d reduce to the constant value of $1/\sqrt{8}$. This might be used in general as an indicator to find the beginning of the self-similar region in limited wake measurements that usually occur in field measurements.

Figure 20(*a*) shows the values of σ_{y_0} predicted by (6.10) for different yaw angles against the ones obtained from the wind tunnel measurements. The comparison shows that the agreement is fairly good, especially for lower yaw angles.

Next, the wake skew angle in the potential core will be determined. Even though the model suggested by Glauert (1926) can estimate the thrust coefficient correctly (Burton *et al.* 1995), it is unable to properly estimate the skew angle of the flow past a yawed rotor. This is due to the fact that this model only takes into account the component of the induced velocity normal to the rotor, and not the tangential one. As a result, this model is expected to overestimate the flow skew angle at the rotor. Based on the vortex theory, however, the induced velocity at a yawed rotor has a tangential component equal to $a\tan(\chi/2)$, where χ is the flow skew angle with respect to the rotor axis (i.e. $\chi = \gamma + \theta$) (Coleman *et al.* 1945). Based on this work, the value of χ at the rotor disk can be approximated by (Burton *et al.* 1995)

$$\chi = \theta + \gamma = (0.6a + 1)\gamma. \tag{6.11}$$

By substituting a in (6.11) with (6.3), the value of θ at the rotor can be found by:

$$\theta \approx \frac{0.3\gamma}{\cos\gamma}(1 - \sqrt{1 - C_T\cos\gamma}). \tag{6.12}$$

Although (6.12) is intended for the estimation of the flow angle only at the rotor disk, it can acceptably predict the flow skew angle even up to a few rotor diameters downstream, as shown in figure 3 by black lines. Thus, we use (6.12) to estimate the flow skew angle for the whole potential core indicated by θ_{c_0} in figure 18. It is noteworthy to mention that previous flow visualizations as well as inverse free wake simulations (Haans *et al.* 2005; Micallef *et al.* 2009) suggest an empirical formula of $\chi = (0.29C_T + 0.96)\gamma$ in the near wake of a yawed rotor. Although the predictions of the mentioned empirical formula are not shown here for the sake of brevity, they are found in good agreement with the predictions of (6.11).

Next, the wake deflection at $x = x_0$, δ_0 will be estimated. As the wake skew angle is assumed to be constant in the potential core, the value of δ_0 is simply equal to $x_0 \tan\theta_{c_0}$ or approximately $x_0\theta_{c_0}$. To estimate the value of x_0, we use a modified version of the hypothesis suggested by Lee & Chu (2012). It was originally used to find the length of the potential core for a round jet in coflow. Before applying this hypothesis for a yawed turbine, however, the interaction of the potential core and surroundings needs to be further elaborated. The difference in the velocity magnitude between these two regions creates a free shear layer between them as shown in figure 18. The velocity in this layer gradually increases from u_0 at the potential core border to u_∞ at the far lateral distance from the wake centre. The velocity distribution in the horizontal plane at hub height for $0 \leqslant x \leqslant x_0$ can be therefore assumed to have the following distribution:

$$\frac{u}{u_\infty} = \begin{cases} 1 - C_0 & \text{if } r \leqslant r_{pc}, \\ 1 - C_0 \mathrm{e}^{-(r-r_{pc})^2/2s^2} & \text{if } r \geqslant r_{pc}, \end{cases} \tag{6.13}$$

where r is the lateral distance from the wake centre, r_{pc} is the potential core radius in the horizontal plane at each x and s denotes the characteristic width of the shear layer. The width of the shear layer increases from $s = 0$ at $x = 0$ to finally $s = \sigma_{y_0}$ at $x = x_0$. For a uniform and laminar incoming flow, Lee & Chu (2012) suggested that a change in width of a shear layer, in a Lagrangian frame of reference (moving with the eddies), is only proportional to the velocity difference between the potential core and unperturbed surroundings. In real situations, however, we know that the incoming turbulence also enhances the flow entrainment and consequently the growth of the shear layer. In this regard, we can generalize the model proposed by Lee & Chu (2012) by writing the variation of the shear layer width in the following form:

$$\frac{1}{u_\infty}\frac{\mathrm{d}s}{\mathrm{d}t} = \frac{u_s}{u_\infty}\frac{\mathrm{d}s}{\mathrm{d}x} = \alpha I + \beta\frac{u_e}{u_\infty}, \tag{6.14}$$

where u_s is the characteristic velocity of the shear layer and is equal to $0.5(u_\infty + u_0)$, $I = \sqrt{\overline{u'^2}}/\bar{u}_h$ is the incoming streamwise turbulence intensity at hub height, u_e denotes the characteristic relative velocity in the shear layer which is equal to $0.5(u_\infty - u_0)$ and α and β are constants. Equation (6.14) can be integrated as follows:

$$\int_0^{\sigma_{y_0}} \mathrm{d}s = \frac{u_\infty}{u_s}\left(\alpha I + \beta\frac{u_e}{u_\infty}\right)\int_0^{x_0} \mathrm{d}x. \tag{6.15}$$

Inserting the values of σ_{y_0}, u_s and u_e in (6.15) and integrating lead to

$$\frac{x_0}{d} = \frac{\cos\gamma\,(1+\sqrt{1-C_T})}{\sqrt{2}[4\alpha I + 2\beta(1-\sqrt{1-C_T})]}. \tag{6.16}$$

In order to use (6.16), values of α and β should first be estimated. The value of β can be determined thanks to the analogy with jet flows. In ideal conditions with no incoming turbulence (i.e. $I = 0$), equation (6.16) predicts a similar value for x_0 as the one reported in studies of jet flows if 2β is equal to 0.154. The value of α can then be found in such a way that (6.16) provides acceptable predictions for x_0 compared with our measured data. Figure 20(*b*) shows the values of x_0 for different cases predicted by (6.16) compared with the values obtained from the wind tunnel measurements. The value of α is chosen 0.58 to have an acceptable agreement with the experimental dataset. The available data are not likely to be sufficient to reliably find constant coefficients of (6.16); nonetheless, the figure shows that (6.16) is able to capture the variation of x_0 for different cases, provided α is properly specified. Indeed, more numerical simulations or wind tunnel measurements are needed to estimate the universal values of α and β. According to (6.16), it can be readily shown that the length of the potential core decreases with increasing thrust coefficient of the turbine, incoming turbulence and yaw angle. It is important to note that (6.16) does not aim to predict the detailed features of the near wake such as the location of the tip vortices' breakdown, but instead it is intended to estimate the length of the hypothetical potential core used for the far-wake modelling. It should be noted that the tip-speed ratio of the turbine and the wake rotation have no contribution in this equation as they have no effects on the far-wake region (Vermeer, Sørensen & Crespo 2003).

7. Model predictions

For the sake of completeness, the final form of the equations, which predict the far-wake velocity for a yawed turbine, is written in the following:

$$\frac{\Delta\bar{u}}{\bar{u}_\infty} = \left(1 - \sqrt{1 - \frac{C_T\cos\gamma}{8(\sigma_y\sigma_z/d^2)}}\right) \mathrm{e}^{-0.5((y-\delta)/\sigma_y)^2} \mathrm{e}^{-0.5((z-z_h)/\sigma_z)^2}, \tag{7.1}$$

where the wake widths in the lateral and vertical directions can be, respectively, found by

$$\left.\begin{aligned} \frac{\sigma_y}{d} &= k_y\frac{(x-x_0)}{d} + \frac{\cos\gamma}{\sqrt{8}}, \\ \frac{\sigma_z}{d} &= k_z\frac{(x-x_0)}{d} + \frac{1}{\sqrt{8}}. \end{aligned}\right\} \tag{7.2}$$

The normalized length of the potential core x_0/d is

$$\frac{x_0}{d} = \frac{\cos\gamma(1+\sqrt{1-C_T})}{\sqrt{2}(\alpha^* I + \beta^*(1-\sqrt{1-C_T}))}, \tag{7.3}$$

where $\alpha^* = 2.32$ and $\beta^* = 0.154$. The normalized wake deflection δ/d is $\theta_{c_0} x/d$ for $x \leqslant x_0$, and for $x > x_0$ it can be determined by

$$\frac{\delta}{d} = \theta_{c_0}\frac{x_0}{d} + \frac{\theta_{c_0}}{14.7}\sqrt{\frac{\cos\gamma}{k_y k_z C_T}}\left(2.9 + 1.3\sqrt{1-C_T} - C_T\right) \times \ln\left[\frac{\left(1.6+\sqrt{C_T}\right)\left(1.6\sqrt{\dfrac{8\sigma_y\sigma_z}{d^2\cos\gamma}} - \sqrt{C_T}\right)}{\left(1.6-\sqrt{C_T}\right)\left(1.6\sqrt{\dfrac{8\sigma_y\sigma_z}{d^2\cos\gamma}} + \sqrt{C_T}\right)}\right], \tag{7.4}$$

where θ_{c_0} is calculated by (6.12). As x approaches to infinity, the wake deflection asymptotes to the constant value of

$$\frac{\delta_\infty}{d} = \theta_{c_0}\frac{x_0}{d} + \frac{\theta_{c_0}}{14.7}\sqrt{\frac{\cos\gamma}{k_y k_z C_T}}\left(2.9 + 1.3\sqrt{1-C_T} - C_T\right)\ln\left(\frac{1.6+\sqrt{C_T}}{1.6-\sqrt{C_T}}\right). \tag{7.5}$$

Figure 21 shows profiles of the wake velocities predicted by (7.1) against the wind tunnel measurements for $\gamma = 0°$, $10°$ and $20°$. To plot the model predictions, the wake growth rate in the vertical direction is assumed to be equal to the one in the horizontal direction (i.e. $k_y = k_z$) as the available velocity data in the z direction are limited. As clearly shown in the figures, the analytical model acceptably predicts the velocity distribution in the wake of a yawed turbine. The prediction on one side of the wake is, however, less accurate for higher yaw angles. This might be due to the fact that the wake velocity profiles are assumed to have a symmetric Gaussian distribution, whereas it was already shown that the velocity profiles are slightly skewed. This simple analytical model can, however, be particularly useful to assess the potential of yaw-angle control strategies for wind farm power optimizations.

It is worth mentioning that the proposed model is likely able to also predict the wake flow of a tilted turbine. In order to do so, the wake deflection δ in (7.1) should simply be reinserted into the Gaussian profile in the z direction, rather than the one in the y direction. However, one must bear in mind that the model should be used cautiously for tilted turbines because if the turbine wake moves towards the ground, its interaction with the ground in the far-wake region cannot be considered negligible.

In addition to providing wake predictions, the proposed model can lead to a better understanding of the effect of different parameters on the turbine wake. For example, figure 22 shows the variation of the normalized wake deflection in the very far-wake region δ_∞/d predicted by the proposed model as a function of the incoming turbulence intensity I and the turbine thrust coefficient C_T for a turbine with $\gamma = 20°$. To calculate the wake deflection, the wake growth rate in the far-wake region is assumed to be linearly proportional to the incoming turbulence intensity as suggested by Johnson *et al.* (2014). It can be seen in the figure that the wake deflection increases with an increase in the thrust coefficient which is consistent with the finding of Jiménez *et al.* (2010). In addition, the figure shows that the wake deflection increases with a decrease in the incoming turbulence. The decrease in the incoming turbulence basically extends the length of the potential core, and it also reduces the flow entrainment in the far-wake region. As a result, the wake deflection increases in this case. This finding suggests that the implementation of

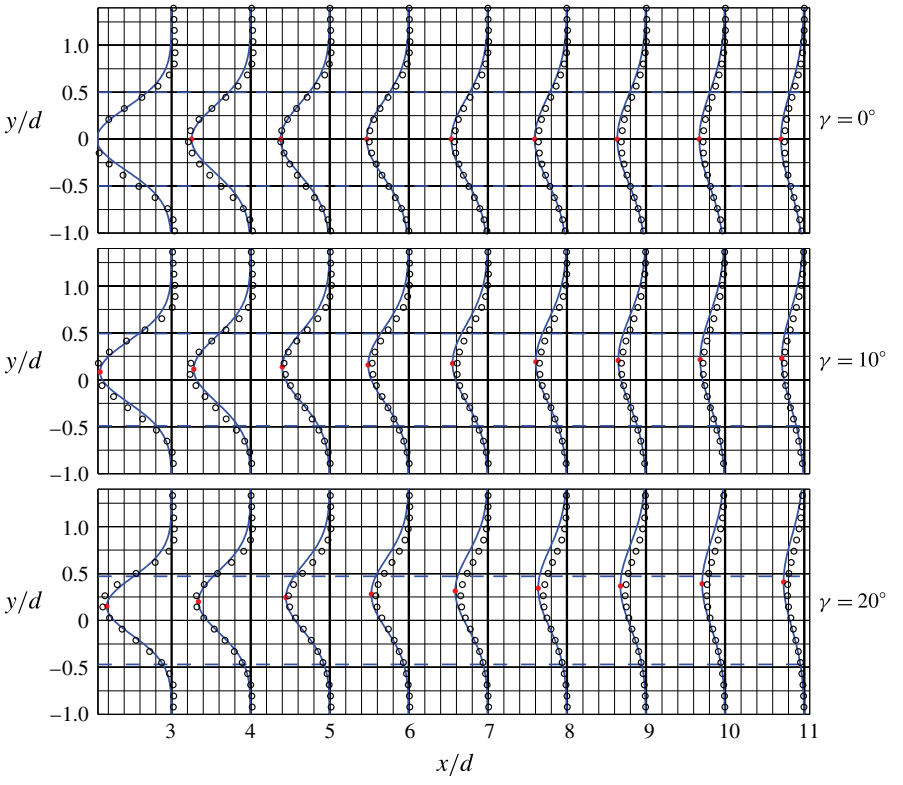

FIGURE 21. Lateral profiles of the normalized streamwise velocity $\bar{u}/\bar{u}_h$ in the wake of a turbine with $\gamma = 0°$, 10° and 20° at $\lambda = \lambda_o$: wind tunnel measurements (open circle), and new proposed model (blue solid line). Red dots show the wake-centre position predicted by the proposed model. Horizontal dashed lines indicate the location of the side tips of the turbine. For each downwind location, $\bar{u}/\bar{u}_h = 1$ on the vertical thick black line. The width of grid squares corresponds to 15 % of $\bar{u}_h$.

yaw-angle control strategies in offshore wind farms, compared to onshore ones, is more promising.

It is important to note that, to estimate the wake characteristics in the onset of the far-wake region, we assumed that the turbine works in the windmill state, i.e. $C_T < 0.96$ (Manwell, McGowan & Rogers 2010). Therefore, the model prediction is not likely to be valid for higher C_T values.

8. Summary

Wind tunnel measurements of the wake of a model wind turbine with different yaw angles (0°, 10°, 20° and 30°) and tip-speed ratios were conducted in a turbulent boundary-layer flow. Power and thrust measurements were performed to study the performance of the wind turbine under these different operating conditions. In general, we found that, as expected, both the generated power and the thrust force of the turbine decrease with the increase of yaw angle. For each yaw angle, high-resolution S-PIV measurements were carried out in a horizontal plane at hub height covering a broad streamwise range (from $0.4d$ to $12d$ downwind of the turbine). The velocity measurements indicate that the wake velocity deficit becomes smaller and

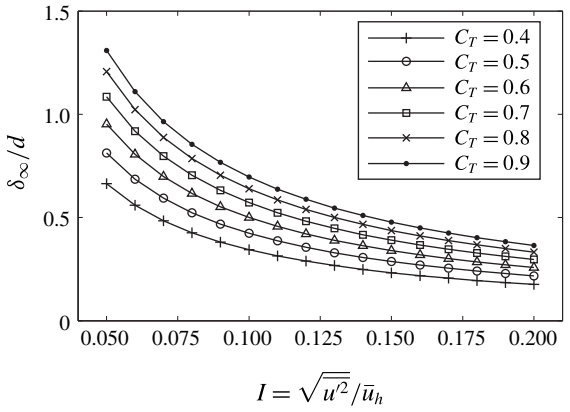

FIGURE 22. Variation of δ_∞/d as a function of the incoming streamwise turbulence intensity $I = \sqrt{\overline{u'^2}}/\bar{u}_h$ for different values of thrust coefficient C_T. The yaw angle γ is assumed to be 20°.

the wake deflection increases with an increase in yaw angle. In another set of S-PIV measurements performed in cross-stream planes, the wake cross-section is quantified at a few selected downwind locations. A CVP is observed in the cross-section of turbine wakes under highly yawed conditions. Moreover, turbine wakes are observed to move upward or downward in these conditions depending on the direction of the yaw angle.

The detailed wind tunnel data were then used to study the budget of the continuity and the RANS equations for the wake of a yawed turbine. The budget study of the continuity equation shows that a strong variation of the spanwise velocity occurring in highly yawed conditions leads to the formation of the CVP. Furthermore, a simple method based on the potential theory is employed to reveal that the vertical displacement of the wake centre under yawed conditions is due to the interaction between the CVP, the ground and the wake rotation. The budget study of the RANS equations points out that the maximum value of the wake skew angle at each downwind location does not occur at the wake centre, but instead it happens where the second derivative of the lateral profile of the streamwise velocity is zero. Our findings show that this asymmetric distribution of the wake skew angle with respect to the wake centre is associated with the origin of the wake deflection for yawed turbines. The integral forms of the RANS equations in both streamwise and spanwise directions were then derived, which provides a solid basis for the development of a simple analytical model to predict the wake flows of yawed turbines.

In the far-wake region of a yawed turbine, self-similarity was examined for both the velocity and skew angle profiles. The results suggest that these profiles can be approximated with a self-similar Gaussian distribution in both spanwise and vertical directions for low yaw angles. The wake growth rate is found to be the same for different yaw angles. This is consistent with the assumption that the far-wake recovery is mainly influenced by incoming flow characteristics, and wind turbine characteristics solely affect the wake properties in the onset of the far-wake region.

The self-similarity analysis along with the budget study of RANS equations enabled us to develop an inexpensive analytical model to predict the velocity distribution in the far wake of a yawed turbine. A new method was employed to estimate the wake

characteristics in the onset of the far-wake region (i.e. where self-similarity holds). An idealized region with a uniform velocity, termed potential core, is assumed downwind of the turbine, analogous with coflowing jets. The potential core shrinks as the wake moves downstream until it eventually fades away, and after that the self-similar region starts to develop. Although the idealized concept of the potential core flow cannot predict the complex three-dimensional structure of the near-wake region, it is shown that it can be successfully employed to provide the necessary information for the beginning of the far-wake self-similar region.

Finally, comparison with the high-resolution wind tunnel measurements shows that the model predictions of the velocity profiles in the wake of a model turbine with different yaw angles are in good agreement with the experimental data. The proposed model can be used as a useful tool to assess the possibility of wind farm power optimization by controlling the yaw angle of turbines. In addition to being a quantitative predictive tool, the proposed model can examine the effect of different turbine and incoming flow characteristics on the wake of a yawed turbine. For instance, a decrease in the incoming turbulence intensity is found to increase wake deflection for a yawed turbine. This suggests that the yaw-angle control has more potential to improve the power production of offshore wind farms, compared with onshore ones.

Acknowledgements

This research was supported by the Swiss National Science Foundation (grant 200021_132122, and grant 206021_144976), the Swiss Federal Office of Energy (grant SI/501337-01), and the Swiss Innovation and Technology Committee (CTI) within the context of the Swiss Competence Center for Energy Research 'FURIES: Future Swiss Electrical Infrastructure'. The first author was also partially supported by the EuroTech Greentech Initiative Wind Energy.

Appendix A

THEOREM 1. *Suppose that the incoming flow is uniform, the flow is extended to infinity in both lateral and vertical directions and the turbine yaw angle is low. Then* $\partial^2\bar{u}/\partial y^2 = 0$ *if* $\partial\theta/\partial y = 0$.

Proof. Writing (3.9) for the lateral position where $\partial\theta/\partial y = 0$ gives

$$\frac{\partial(\bar{w}/\bar{u})}{\partial z} = -\frac{\nu_T}{\bar{u}^2}\frac{\partial^2\bar{u}}{\partial y^2} - \frac{\nu_T}{\bar{u}^2}\frac{\partial^2\bar{u}}{\partial z^2}. \tag{A 1}$$

Integrating (A 1) with respect to z from $-\infty$ to ∞ yields

$$\frac{\bar{w}}{\bar{u}}\bigg|_{z=-\infty}^{+\infty} = -\nu_T \int_{-\infty}^{\infty} \frac{1}{\bar{u}^2}\frac{\partial^2\bar{u}}{\partial y^2}\,\mathrm{d}z - \nu_T \int_{-\infty}^{\infty} \frac{1}{\bar{u}^2}\frac{\partial^2\bar{u}}{\partial z^2}\,\mathrm{d}z. \tag{A 2}$$

The left-hand side of (A 2) can be neglected as $\bar{w}/\bar{u}$ vanishes at large values of z. Next, let $\bar{u}_\infty$ and $\bar{u}_c$ denote the incoming velocity and the velocity at the wake centre, respectively. Then,

$$\frac{1}{\bar{u}_c^2}\frac{\partial^2\bar{u}}{\partial z^2} \geqslant \frac{1}{\bar{u}^2}\frac{\partial^2\bar{u}}{\partial z^2} \geqslant \frac{1}{\bar{u}_\infty^2}\frac{\partial^2\bar{u}}{\partial z^2}. \tag{A 3}$$

Integrating (A 3) with respect to z from $-\infty$ to ∞ leads to

$$\frac{1}{\bar{u}_c^2}\frac{\partial \bar{u}}{\partial z}\bigg|_{z=-\infty}^{+\infty} \geqslant \int_{-\infty}^{\infty}\frac{1}{\bar{u}^2}\frac{\partial^2 \bar{u}}{\partial z^2}\,\mathrm{d}z \geqslant \frac{1}{\bar{u}_\infty^2}\frac{\partial \bar{u}}{\partial z}\bigg|_{z=-\infty}^{+\infty}. \tag{A 4}$$

The middle term in (A 4) has to be equal to zero as both side terms are equal to zero, which in turn suggests that the second term on the right-hand side of (A 2) is also equal to zero. Hence, from (A 2),

$$\int_{-\infty}^{\infty}\frac{1}{\bar{u}^2}\frac{\partial^2 \bar{u}}{\partial y^2}\,\mathrm{d}z = 0. \tag{A 5}$$

Now, assume that $\bar{u}$ at each x has the form of the product,

$$\bar{u} = \phi(y)\psi(z), \tag{A 6}$$

where both $\phi(y) \geqslant 0$ and $\psi(z) \geqslant 0$ for all the values of y and z. Although (A 6) is unlikely to be valid for wakes of turbines with high yaw angles, it is an acceptable assumption for wakes of turbines with low yaw angles where the wake cross-section can be approximated by a two-dimensional Gaussian function found in (5.1). From (A 6), we can write

$$\frac{\partial^2 \bar{u}}{\partial y^2} = \phi''(y)\psi(z). \tag{A 7}$$

Based on (A 7), we conclude that the sign of $\partial^2\bar{u}/\partial y^2$ in the given lateral position does not change from $z=-\infty$ to ∞ (i.e. it is strictly non-negative or non-positive). Therefore, $\partial^2\bar{u}/\partial y^2$ has to be zero in order to satisfy (A 5).

Appendix B

This appendix contains the algebraic manipulations needed for the estimation of the wake deflection δ. In order to find the trajectory of the wake centre, θ_c in (5.7) should be replaced with $\mathrm{d}y/\mathrm{d}x$, then (5.7) can be integrated to find the wake deflection δ at each x. To make the integration simpler, the product of $\sigma_y\sigma_z$ is approximated by $\bar{\sigma}^2$ which is defined as

$$\bar{\sigma} = \bar{k}(x - x_0) + \bar{\sigma}_0, \tag{B 1}$$

where $\bar{k} = \sqrt{k_y k_z}$ and $\bar{\sigma}_0 = \sqrt{\sigma_{y_0}\sigma_{z_0}}$. Note that $\bar{\sigma}^2$ is exactly equal to $\sigma_y\sigma_z$ if $k_y\sigma_{z_0} = k_z\sigma_{y_0}$. Moreover, C in the right-hand side of (5.7) should be substituted by (5.4) which gives

$$\begin{aligned} C^2 - 3\mathrm{e}^{1/12}C + 3\mathrm{e}^{1/3} &= [2 + 3(\mathrm{e}^{1/3} - \mathrm{e}^{1/12})] - \frac{\bar{\sigma}_0^2 M_0}{\bar{\sigma}^2} + (3\mathrm{e}^{1/12} - 2)\sqrt{1 - \frac{\bar{\sigma}_0^2 M_0}{\bar{\sigma}^2}} \\ &\approx 2.93 - \frac{\bar{\sigma}_0^2 M_0}{\bar{\sigma}^2} + 1.26\sqrt{1 - \frac{\bar{\sigma}_0^2 M_0}{\bar{\sigma}^2}}. \end{aligned} \tag{B 2}$$

$\sqrt{1 - (\bar{\sigma}_0^2 M_0/\bar{\sigma}^2)}$ in the above equation can be replaced with $(1 - (\bar{\sigma}_0^2 M_0/2\bar{\sigma}^2))$ as $\bar{\sigma}$ quickly grows in the far wake (note that $\sqrt{1-x}$ asymptotes to $(1 - 0.5x)$ as $x \to 0$). Equation (B 2) is therefore simplified to

$$C^2 - 3\mathrm{e}^{1/12}C + 3\mathrm{e}^{1/3} \approx 1.6\left(2.6 - \frac{\bar{\sigma}_0^2 M_0}{\bar{\sigma}^2}\right). \tag{B 3}$$

Now, inserting (B 3) into (5.7) and replacing θ_c with $\mathrm{d}y/\mathrm{d}x$ enables us to find the wake deflection δ:

$$\int_{\delta_0}^{\delta} \mathrm{d}y \approx \frac{\theta_{c_0}\bar{\sigma}_0^2 E_0}{1.6\bar{k}} \int_{\bar{\sigma}_0}^{\bar{\sigma}} \frac{\mathrm{d}\hat{\sigma}}{2.6\hat{\sigma}^2 - \bar{\sigma}_0^2 M_0}, \tag{B 4}$$

where $\mathrm{d}x$ is replaced with $\mathrm{d}\hat{\sigma}/\bar{k}$. Performing the integration leads to

$$\delta \approx \delta_0 + \frac{\theta_{c_0}\bar{\sigma}_0 E_0}{2.6\bar{k}\sqrt{M_0}} \left[\operatorname{arctanh}\left(\frac{1.6}{\sqrt{M_0}}\right) - \operatorname{arctanh}\left(\frac{1.6}{\sqrt{M_0}}\frac{\bar{\sigma}}{\bar{\sigma}_0}\right)\right]. \tag{B 5}$$

After using hyperbolic trigonometric identities, (B 5) can be simplified to

$$\delta \approx \delta_0 + \frac{\theta_{c_0}\bar{\sigma}_0 E_0}{5.2\bar{k}\sqrt{M_0}} \ln\left[\frac{(1.6+\sqrt{M_0})\left(1.6\dfrac{\bar{\sigma}}{\bar{\sigma}_0} - \sqrt{M_0}\right)}{(1.6-\sqrt{M_0})\left(1.6\dfrac{\bar{\sigma}}{\bar{\sigma}_0} + \sqrt{M_0}\right)}\right]. \tag{B 6}$$

REFERENCES

ABKAR, M. & PORTÉ-AGEL, F. 2013 The effect of free-atmosphere stratification on boundary-layer flow and power output from very large wind farms. *Energies* **6** (5), 2338–2361.

ABKAR, M. & PORTÉ-AGEL, F. 2015 Influence of atmospheric stability on wind-turbine wakes: a large-eddy simulation study. *Phys. Fluids* **27** (3), 035104.

ABRAHAM, G. 1970 The flow of round buoyant jets issuing vertically into ambient fluid flowing in a horizontal direction. In *5th International Water Pollution Research Conference, July–August, San Francisco*. Pergamon.

AMOURA, Z., ROIG, V., RISSO, F. & BILLET, A. 2010 Attenuation of the wake of a sphere in an intense incident turbulence with large length scales. *Phys. Fluids* **22** (5), 055105.

BAGCHI, P. & BALACHANDAR, S. 2004 Response of the wake of an isolated particle to an isotropic turbulent flow. *J. Fluid Mech.* **518**, 95–123.

BASTANKHAH, M. & PORTÉ-AGEL, F. 2014 A new analytical model for wind-turbine wakes. *Renew. Energy* **70**, 116–123.

BROADWELL, J. E. & BREIDENTHAL, R. E. 1984 Structure and mixing of a transverse jet in incompressible flow. *J. Fluid Mech.* **148**, 405–412.

BURTON, T., SHARPE, D., JENKINS, N. & BOSSANYI, E. 1995 *Wind Energy Handbook*, 1st edn. Wiley.

CAL, R. B., LEBRÓN, J., CASTILLO, L., KANG, H. S. & MENEVEAU, C. 2010 Experimental study of the horizontally averaged flow structure in a model wind-turbine array boundary layer. *J. Renew. Sustain. Energy* **2**, 013106.

CALAF, M., MENEVEAU, C. & MEYERS, J. 2010 Large eddy simulation study of fully developed wind-turbine array boundary layers. *Phys. Fluids* **22** (1), 015110.

COLEMAN, R. P., FEINGOLD, A. M. & STEMPIN, C. W. 1945 Evaluation of the induced-velocity field of an idealized helicoptor rotor. *Tech Rep.* DTIC Document.

CORTELEZZI, L. & KARAGOZIAN, A. R. 2001 On the formation of the counter-rotating vortex pair in transverse jets. *J. Fluid Mech.* **446**, 347–373.

DAHLBERG, J. Å. & MEDICI, D. 2003 Potential improvement of wind turbine array efficiency by active wake control (awc). In *Proceedings of the European Wind Energy Conference and Exhibition*, pp. 65–84. EWEA.

DUFRESNE, N. P. & WOSNIK, M. 2013 Velocity deficit and swirl in the turbulent wake of a wind turbine. *Mar. Technol. Soc. J.* **47** (4), 193–205.

EAMES, I., JOHNSON, P. B., ROIG, V. & RISSO, F. 2011*a* Effect of turbulence on the downstream velocity deficit of a rigid sphere. *Phys. Fluids* **23** (9), 095103.

EAMES, I., JONSSON, C. & JOHNSON, P. B. 2011*b* The growth of a cylinder wake in turbulent flow. *J. Turbul.* **12** (9), 1–16.

FAN, L. N. 1967 Turbulent buoyant jets into stratified or flowing ambient fluids. *Tech Rep.*, W. M. Keck Laboratory of Hydraulics and Water Resources.

FLEMING, P. A., GEBRAAD, P. M. O., LEE, S., VAN WINGERDEN, J., JOHNSON, K., CHURCHFIELD, M., MICHALAKES, J., SPALART, P. & MORIARTY, P. 2014 Evaluating techniques for redirecting turbine wakes using SOWFA. *Renew. Energy* **70**, 211–218.

FRANDSEN, S. T., BARTHELMIE, R., PRYOR, S., RATHMANN, O., LARSEN, S., HØJSTRUP, J. & THØGERSEN, M. 2006 Analytical modelling of wind speed deficit in large offshore wind farms. *Wind Energy* **9**, 39–53.

GEBRAAD, P. M. O., TEEUWISSE, F. W., WINGERDEN, J. W., FLEMING, P. A., RUBEN, S. D., MARDEN, J. R. & PAO, L. Y. 2014 Wind plant power optimization through yaw control using a parametric model for wake effects – a CFD simulation study. *Wind Energy* **19**, 95–114.

GLAUERT, H. 1926 *A General Theory of the Autogyro*. HM Stationery Office.

GRANT, I. & PARKIN, P. 2000 A DPIV study of the trailing vortex elements from the blades of a horizontal axis wind turbine in yaw. *Exp. Fluids* **28** (4), 368–376.

GRANT, I., PARKIN, P. & WANG, X. 1997 Optical vortex tracking studies of a horizontal axis wind turbine in yaw using laser-sheet, flow visualisation. *Exp. Fluids* **23** (6), 513–519.

HAANS, W. 2011 Wind turbine aerodynamics in yaw: unravelling the measured rotor wake. PhD thesis, TU Delft, Delft University of Technology.

HAANS, W., VAN KUIK, G. & VAN BUSSEL, G. J. W. 2007 Experimentally observed effects of yaw misalignment on the inflow in the rotor plane. *J. Phys. Conf. Ser.* **75**, 012012.

HAANS, W., SANT, T., VAN KUIK, G. & VAN BUSSEL, G. 2005 Measurement and modelling of tip vortex paths in the wake of a HAWT under yawed flow conditions. In *43th AIAA Aerospace Sciences Meeting and Exhibit*, pp. 136–145.

HOWLAND, M. F., BOSSUYT, J., A., MARTÍNEZ-TOSSAS L., MEYERS, J. & MENEVEAU, C. 2016 Wake structure in actuator disk models of wind turbines in yaw under uniform inflow conditions. *J. Renew. Sustain. Energy* **8**, 043301.

JENSEN, N. O. 1983 A note on wind turbine interaction. *Tech Rep.* Ris-M-2411. Risoe National Laboratory, Roskilde, Denmark.

JIMÉNEZ, Á., CRESPO, A. & MIGOYA, E. 2010 Application of a LES technique to characterize the wake deflection of a wind turbine in yaw. *Wind Energy* **13** (6), 559–572.

JOHANSSON, P. B. V., GEORGE, W. K. & GOURLAY, M. J. 2003 Equilibrium similarity, effects of initial conditions and local Reynolds number on the axisymmetric wake. *Phys. Fluids* **15** (3), 603–617.

JOHNSON, P. B., JONSSON, C., ACHILLEOS, S. & EAMES, I. 2014 On the spread and decay of wind turbine wakes in ambient turbulence. *J. Phys. Conf. Ser.* **555**, 012055.

KELSO, R. M., LIM, T. T. & PERRY, A. E. 1996 An experimental study of round jets in cross-flow. *J. Fluid Mech.* **306**, 111–144.

KIKKERT, G. A. 2006 Buoyant jets with two and three-dimensional trajectories. PhD thesis, University of Canterbury.

KROGSTAD, P. & ADARAMOLA, M. S. 2012 Performance and near wake measurements of a model horizontal axis wind turbine. *Wind Energy* **15** (5), 743–756.

LEE, J. H. & CHU, V. 2012 *Turbulent Jets and Plumes: A Lagrangian Approach*. Springer.

LEGENDRE, D., MERLE, A. & MAGNAUDET, J. 2006 Wake of a spherical bubble or a solid sphere set fixed in a turbulent environment. *Phys. Fluids* **18** (4), 048102.

LISSAMAN, P. B. S. 1979 Energy effectiveness of arbitrary arrays of wind turbines. *J. Energy* **3** (6), 323–328.

LU, H. & PORTÉ-AGEL, F. 2011 Large-eddy simulation of a very large wind farm in a stable atmospheric boundary layer. *Phys. Fluids* **23** (6), 065101.

MAHESH, K. 2013 The interaction of jets with crossflow. *Annu. Rev. Fluid Mech.* **45**, 379–407.

MANWELL, J. F., MCGOWAN, J. G. & ROGERS, A. L. 2010 *Wind Energy Explained: Theory, Design and Application*. Wiley.

MARZOUK, Y. M. & GHONIEM, A. F. 2007 Vorticity structure and evolution in a transverse jet. *J. Fluid Mech.* **575**, 267–305.

MEDICI, D. & ALFREDSSON, P. 2006 Measurement on a wind turbine wake: 3D effects and bluff body vortex shedding. *Wind Energy* **9**, 219–236.

MICALLEF, D., BUSSEL, G., FERREIRA, C. S. & SANT, T. 2013 An investigation of radial velocities for a horizontal axis wind turbine in axial and yawed flows. *Wind Energy* **16** (4), 529–544.

MICALLEF, D., FERREIRA, C. S., SANT, T. & VAN BUSSEL, G. 2009 Wake skew angle variation with rotor thrust for wind turbines in yaw based on the mexico experiment. In *5th PhD Seminar on Wind Energy in Europe*. EAWE.

MUPPIDI, S. & MAHESH, K. 2006 Two-dimensional model problem to explain counter-rotating vortex pair formation in a transverse jet. *Phys. Fluids* **18** (8), 085103.

OKULOV, V. L., NAUMOV, I. V., MIKKELSEN, R. F. & SØRENSEN, J. N. 2015 Wake effect on a uniform flow behind wind-turbine model. *J. Phys. Conf. Ser.* **625**, 012011.

OOMS, G. 1972 A new method for the calculation of the plume path of gases emitted by a stack. *Atmos. Environ.* **6** (12), 899–909.

POPE, S. B. 2000 *Turbulent Flows*. Cambridge University Press.

PORTÉ-AGEL, F., WU, Y. T. & CHEN, C. H. 2013 A numerical study of the effects of wind direction on turbine wakes and power losses in a large wind farm. *Energies* **6** (10), 5297–5313.

RAJARATNAM, N. 1976 *Turbulent Jets*. Elsevier.

SANT, T. 2007 Improving BEM-based aerodynamic models in wind turbine design codes. PhD thesis, Delft University of Technology.

SØRENSEN, J. N. 2015 *General Momentum Theory for Horizontal Axis Wind Turbines*. Springer.

TENNEKES, H. & LUMLEY, J. L. 1972 *A First Course in Turbulence*. MIT.

VERMEER, L., SØRENSEN, J. & CRESPO, A. 2003 Wind turbine wake aerodynamics. *Prog. Aerosp. Sci.* **39**, 467–510.

VERMEULEN, P. E. J. 1980 An experimental analysis of wind turbine wakes. In *3rd International Symposium on Wind Energy Systems*, pp. 431–450. Lyngby.

WANG, X. & KIKKERT, G. A. 2014 Behaviour of oblique jets released in a moving ambient. *J. Hydraul. Res.* **52** (4), 490–501.

WHITE, F. M. 2009 *Fluid Mechanics*. McGraw-Hill.

WU, J. S. & FAETH, G. M. 1994 Sphere wakes at moderate Reynolds numbers in a turbulent environment. *AIAA J.* **32** (3), 535–541.

XIE, S. & ARCHER, C. 2015 Self-similarity and turbulence characteristics of wind turbine wakes via large-eddy simulation. *Wind Energy* **18**, 1815–1838.